Modeling of temperature- and strain-driven intermetallic compound evolution in an Al–Mg system via a multiphase-field approach with application to refill friction stir spot welding

Syed Hasan Raza [a,*], Tobias Mittnacht [b,*], George Diyoke [d], Daniel Schneider [b,c], Britta Nestler [b,c], Benjamin Klusemann [a,d]

[a] *Institute of Product and Process Innovation, Leuphana University Lüneburg, Lüneburg, Germany*
[b] *Institute of Applied Materials (IAM-MMS), Karlsruhe Institute of Technology (KIT), Karlsruhe, Germany*
[c] *Institute of Digital Materials (IDM), Karlsruhe University of Applied Sciences, Karlsruhe, Germany*
[d] *Solid State Materials Processing, Institute of Materials Mechanics, Helmholtz-Zentrum Hereon, Geesthacht, Germany*

ARTICLE INFO

Keywords:
Multiphase-field method
Chemo-mechanical coupling
Intermetallic compound
Al–Mg system
Solid-state joining process

ABSTRACT

The prospect of joining dissimilar materials via solid-state processes presents an opportunity to obtain multi-material structures having a synergy of desirable properties of the joined materials. However, the issue of the formation of intermetallic compounds at the weld interface of dissimilar materials arises with that, depending upon the temperature and pressure conditions as per phase diagram. As the thickness of the intermetallic compounds may determine the mechanical properties of the joint, understanding the driving mechanisms and evolution of these intermetallic compounds in solid-state joining processes, such as refill friction stir spot welding (refill FSSW), is crucial. In this contribution, we account for the effect of different driving forces in a multiphase-field approach and investigate the evolution of the intermetallic compounds driven by chemical and mechanical forces. A finite-element simulation of the refill FSSW is pursued to obtain the peak temperature and strain at different locations of the weld interface. The microstructure simulations obtained via the multiphase-field model give insight into the morphology and kinetics evolution of the intermetallic compounds for both, the absence of strain (purely chemically-driven model) as well as presence of strain (chemo-mechanically-driven model). The consideration of strain proves to result in thicker intermetallic compound layer. Furthermore, the impact of interface energy and initial grain configuration is found to be significant on the overall intermetallic compounds evolution.

1. Introduction

The transport industry, such as automotive and aerospace, demands materials that combine low density, high specific strength, good corrosion resistance, good workability, high thermal and electrical conductivity, attractive appearance, and inherent recy clability. Aluminum and magnesium partially address these demands (Liu et al., 2014) and combining the two materials presents research opportunities into technologies for the production of dissimilar Al/Mg joints. When traditional fusion welding techniques are used to produce Al/Mg joints, excessive brittle intermetallic phases are formed at the weld (Liu et al., 2014). Solid state joining processes, on the other hand, bond two materials in solid state, allowing the possibility of obtaining defect free welds with superior

* Corresponding authors.
E-mail addresses: shasanrr@gmail.com (S.H. Raza), tobiasmittnacht@gmail.com (T. Mittnacht).

properties. Furthermore, joining two materials in solid state prevents metallurgical reactions at melting and solidification, resulting for instance in joints without pores. The formation of an excessive intermetallic compound at the weld interface could lead to inferior mechanical properties (Yan et al., 2005). The excessive thickness of the intermetallic layer leads to brittleness of the joint interface, causing easier crack initiation and propagation (Chen et al., 2006). Since the temperatures reached during solid state joining are at most 80% of the melting temperature, the growth of intermetallic compounds is relatively controlled (Liu et al., 2014; Plaine et al., 2015).

Refill Friction Stir Spot Welding (refill FSSW) (Schilling and dos Santos, 2004; Yang et al., 2014) is a relatively new solid state joining process, which has successfully been used to join similar (Rosendo et al., 2011; Campanelli et al., 2013; Effertz et al., 2016) and dissimilar materials (Lee et al., 2009; Gerlich et al., 2005; Tozaki et al., 2007; Liyanage et al., 2009), which are difficult to weld via conventional methods. The tool consists of three parts: a sleeve, a pin, and a clamping ring. The tool is placed on the two workpieces being joined, i.e., typically two material sheets in lap joint configuration, and the clamping ring clamps them against a backing. The process starts with the pin and sleeve rotation that plasticizes the material beneath, followed by the plunging stage. During the plunging stage, the sleeve rotates and penetrates into the top sheet while the pin moves in the opposite direction, creating a cavity for plasticized material displaced by the sleeve to move into. Once the sleeve reaches the target depth, typically near but above the interface, the dwelling stage starts where the sleeve keeps rotating without any further translation. At the end of the dwelling stage, both the sleeve and pin move to their original position, i.e., the pin pushes the material back, and thus the joint is obtained. During refill FSSW, the weld region of two joined materials is subjected to frictional heating and severe plastic deformation. In the case of joining dissimilar materials, intermetallic compounds tend to form at the interface affecting the weld strength. Suhuddin et al. (2014) studied the formation and evolution of Al_3Mg_2 and $Al_{12}Mg_{17}$ intermetallic compounds by joining Al and Mg alloys via refill FSSW. They observed variable intermetallic compound thickness across the weld interface, being thicker at the position of high strain and thinner otherwise. The authors concluded that the driving mechanism for the intermetallic phases is not just temperature but also material flow. Furthermore, the authors found a reduction in the lap shear strength of the joints due to the distribution of the intermetallic compound layer. In another study, Yamamoto et al. (2009) produced Al/Mg joints via friction stir welding (FSW) and found the formation of Al_3Mg_2 and $Al_{12}Mg_{17}$ intermetallic compounds at the weld interface as well. The authors declared that the intermetallic layer thickness mainly affects the tensile strength of the produced joints. The increasing thickness of the intermetallic layer weakens the mechanical interlocking leading to decreasing tensile strength. Chen et al. (2021) also observed the formation of Al_3Mg_2 and $Al_{12}Mg_{17}$ intermetallic compounds during FSW of Al and Mg. The authors successfully improved the joint strength by reducing the thickness of the intermetallic compounds by optimizing the process parameters. To produce welds of superior quality, understanding the driving mechanisms and the evolution of intermetallic compounds is essential (McLean et al., 2003).

The complex nature of solid state processes, such as refill FSSW, makes it difficult to investigate it solely by experiments. Furthermore, since experiments tend to be expensive and time consuming, numerical methods are employed to overcome these challenges (Meyghani et al., 2017) and to get further physical insight. For instance, a process simulation based on the finite element method (FEM) can provide the temperature, strain, and strain rate profile at the weld interface, which are important driving factors for the formation and evolution of intermetallic compounds. Different algorithms of continuum mechanics are available, leading to several numerical studies to investigate friction based joining techniques. Meyghani et al. (2017) reviewed different numerical approaches for the investigation of FSW and concluded that the Lagrangian method is most suitable for thermal modeling while the Eulerian method more for modeling the material flow. The two methods can also be coupled to obtain a single numerical approach, known as Arbitrary Lagrangian Eulerian (ALE) approach, which is an appropriate approach for modeling large plastic deformation problems (Meyghani et al., 2017). Awang and Mucino (2010) implemented a fully coupled three dimensional FE model of the FSSW process and successfully predicted the peak temperature as per theoretical studies. The authors studied the energy generated during the process and the effect of various process parameters on it, concluding that the frictional work between the tool and the interface generates the most energy during the process, and rotational tool speed plays a direct role in yielding frictional dissipation energy. The material flow during the refill FSSW was studied by Ji et al. (2017a,b) via a three dimensional finite volume model and it is concluded that the maximum material flow velocity takes place at the sleeve's outer wall, which decrease moving radially away from the tool center, impacting grain sizes in various welding zones. The authors also compared the effect of a groove on the sleeve and the size of the sleeve's outer diameter on the material flow during the process. Recently, Janga et al. (2021) also developed a thermo mechanical refill FSSW model in DEFORM3D and validated it via experimental investigations. The model was validated by evaluating the points analogous to the thermocouples location in the experiments and comparing the obtained thermal cycles. The developed model is capable of predicting thermal cycles, material flow, and strain distribution in the weld zone. To this end, the temperature and strain experienced at the weld interface can be obtained from such thermo mechanical process simulations and used as boundary condition for studying the microstructure evolution of the intermetallic compounds that form at the weld interface.

The multiphase field method is a widely used approach for the investigation of evolving microstructures (Steinbach et al., 1996) and is applied to obtain temporal and spatial evolution of intermetallic compounds. The approach is based on a functional expression (e.g. energy density, entropy density, grand chemical potential) that describes the evolution of microstructure, regardless of the number of domains, and requires no explicit interface tracking (Qin and Bhadeshia, 2010). Multiphase field methods treat the microstructural evolution in terms of bulk and interface domains (Chen, 2002) with the help of two sets of field variables: conserved and non conserved, which are functions of space and time (Moelans et al., 2008). Conserved variables satisfy local conservation conditions (Chen, 2002), whereas the non conserved variables do not. Local composition or concentration are examples of conserved variables. Non conserved variables are further classified into order parameters and phase fields. The order parameters represent, for

instance, local (crystal) structure/orientation, whereas the phase fields indicate the presence of a specific grain or phase (Moelans et al., 2008). The distinction between two ordering states, e.g., solid and liquid phases or two grains, is represented by the phase fields being non zero in a particular region and zero otherwise. For systems involving multiple phases, a multiphase field framework is applicable, where it is ensured that at each local point, the sum of all phase field variables is one (Steinbach et al., 1996). The variation of phase fields across the interface of two phases (or grains) is considered to be diffuse. In the phase field method, multiple driving forces for the microstructural evolution can be incorporated by adding their corresponding energy contributions in formulating the total energy function. The energy is formulated by using either a free energy (Steinbach and Pezzolla, 1999) or grand chemical potential functional (Choudhury and Nestler, 2012). In contrast to a free energy functional, the grand chemical potential approach (Choudhury and Nestler, 2012; Plapp, 2011; Hötzer et al., 2015) essentially maps the thermodynamic energies in the grand potential space instead of free energies. Choudhury and Nestler (2012) showed that doing so decouples the interface energy and interface thickness, making the grid resolution independent of the driving forces and thus enabling an efficient simulation of large scale domains. Regardless of the space used to map the thermodynamic energies, the essential energy contributions to the total potential are the bulk (chemical) and interface energies, with the possibility of adding contributions such as mechanical and electrical contributions, depending upon the problem. The CALPHAD (CALculation of PHAse Diagram) approach, based on computational thermodynamics, can be used for a quantitative computation of the bulk contributions. For instance, for a specific material system, the Gibbs free energy contributions of each thermodynamic phase are taken from CALPHAD data sets and used as input data for the phase field model. Once the field variables and total energy potential are set, Cahn Hilliard nonlinear diffusion continuum equation (Cahn and Allen, 1977) is used to describe the temporal evolution of composition fields and the Allen Cahn (time dependent Ginzburg Landau) equation defines the evolution of the phase fields (Chen, 2002).

Multiphase field methods have been successfully used in various applications such as solidification (Nomura et al., 2010; Böttger et al., 2012; Minamoto et al., 2010), grain growth (Schaffnit et al., 2007; Apel et al., 2009), fracture mechanics (Schneider et al., 2016; Nguyen et al., 2017), along with solid state phase transformations (Steinbach and Apel, 2006; Militzer and Azizi Alizamini, 2011; Nakajima et al., 2006). Evolution of intermetallic compounds in a Cu Sn system during soldering via the phase field method was studied by Park and Arroyave (2010) and Huh et al. (2004). Park and Arroyave (2010) incorporated a nucleation model based on Poisson's distribution with the phase field model that was coupled with CALPHAD. The intermetallic compound formation and kinetics obtained with the simulation agreed well with the experimental results. Using the multiphase field framework, Huh et al. (2004) investigated the effect of grain boundary diffusion on the intermetallic compound evolution. Yang et al. (2021) predicted the intermetallic compound thickness during FSW of an Al Mg system by developing an atomic diffusion model. Their approach involved a thermo mechanical model to predict the temperature and strain rate at the weld interface, which are used to compute the dislocation density and diffusion coefficient via a micro scale model to predict the intermetallic compound thickness. The authors concluded that the dislocation density could expedite the diffusion coefficients, leading to higher intermetallic compound thickness. Raza and Klusemann (2020) presented a multiphase field model formulated in terms of free energy functional to investigate the evolution of the intermetallic compounds Al_3Mg_2 and $Al_{12}Mg_{17}$ driven by temperature in an Al Mg system. However, to complete the framework regarding the evolution of intermetallic compounds in thermo mechanical processes such as solid state joining, the contribution of strain must be taken into account alongside temperature. Motivated by this, the current study presents first a finite element simulation of refill FSSW to obtain the temperature and strain information, including the strain rate, at the weld interface. The quantities are then used as boundary conditions for the proposed multiphase field approach, accounting for temperature and strain effects, to investigate the intermetallic compound evolution in an Al/Mg weld. This is a crucial step in understanding the evolution of intermetallic compounds during processes like refill FSSW.

The structure of this paper is as follows: In Section 2, the theoretical background of the employed multiphase field model, including strain energy contributions as per Schneider et al. (2018), Amos et al. (2018) and Schoof et al. (2020) are presented. Furthermore, the computation of the required physical parameters for the multiphase field model from the CALPHAD assessment is illustrated. In Section 3, at first, the setup for the process simulation of the refill FSSW process based on the finite element method is presented. Afterwards, the considered initial microstructure for the multiphase field approach is shown. Section 4 exhibits the finite element simulation results of the refill FSSW process in terms of the temperature and strain at the weld interface. Taking the output of the process simulation as an input for the multiphase field model, the evolution of the intermetallic compounds driven by temperature and strain is investigated. Finally, Section 5 concludes this contribution. A schematic for clarification is presented in Fig. 1.

2. Theory

Phase field models consider different thermodynamic potentials to describe the driving forces of phase transition. In the following, a synopsis of the fundamental equations of the purely chemical model, followed by the incorporation of the strain energy contribution to the total free energy of the multiphase field model is presented.

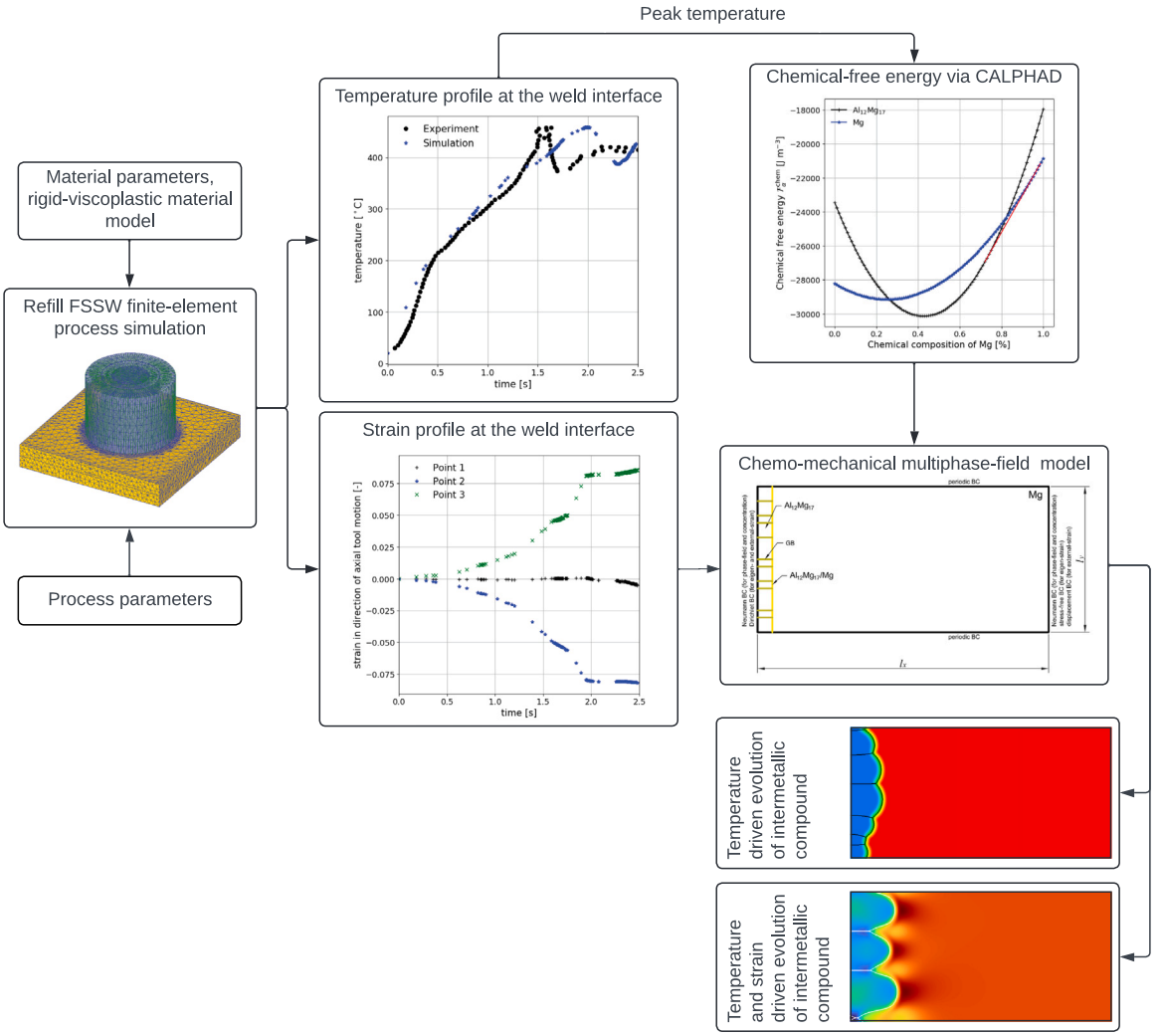

Fig. 1. Schematic of the paper: The material and process parameters are used from literature to simulate the refill FSSW process. The temperature and strain profiles obtained from the process simulation and the chemical-free energy via CALPHAD are inputs for the chemo-mechanical multiphase-field model. The chemo-mechanical model gives the evolution of intermetallic compound driven solely by temperature or combined thermo-mechanics..

2.1. Multiphase field model

Let[1] $\boldsymbol{\phi} = \{\phi_0, \dots, \phi_\alpha, \dots \phi_N\}$ be a N tuple with N denoting the total number of phases and $\phi_\alpha = \phi_\alpha(\boldsymbol{x}, t)$ representing the spatial distribution $\boldsymbol{x}$ of each phase α at time t as a non conserved field variable and $\boldsymbol{c}_\alpha = \{c_{\alpha,0}, \dots, c_{\alpha,i}, \dots, c_{\alpha,K}\}$ be the conserved field variable denoting the spatial composition of K components at time t as a tuple. The phase field variable ϕ_α can be considered as the local volume fraction of the phase (or grain) α designated by the subscript. The phase field variables are subjected to the following constraint at any position in the system (Nestler et al., 2005)

$$\sum_{\alpha=1}^{N} \phi_\alpha(\boldsymbol{x}, t) = 1\,. \tag{1}$$

[1] The following notation is used: Definitions are denoted by $:=$. Assuming a, b, c, and d as scalars, and $\boldsymbol{e}$ and $\boldsymbol{f}$ as vectors, $c = a \cdot b$ and $d = \boldsymbol{e} \cdot \boldsymbol{f}$ represent the dot product. $\nabla(\bullet)$ designates the gradient operator, $\nabla \cdot (\bullet)$ designates the divergence operator, and $\ln(\bullet)$ represents the natural logarithm. $\dot{[\bullet]}$ represents the time derivative $|\bullet|$ denotes the magnitude of $[\bullet]$ while $[\![\bullet]\!]$ the jump of $[\bullet]$ across the interface. Square brackets $[\dots]$ are used to collect mathematical expressions and components in explicit vector and matrix representations whereas round brackets $(\dots)$ represent function arguments.

Eq. (1) ensures that the sum of all the phase field variables equals one even though each phase field variable varies between zero and one at the interfaces (and grain boundaries). The constraints on the composition field variables read

$$\sum_{\alpha=1}^{N} h_\alpha(\boldsymbol{\phi}) c_{\alpha,i}(\boldsymbol{x},t) = c_i(\boldsymbol{x},t)\,, \tag{2}$$

$$\sum_{i=1}^{K} c_i(\boldsymbol{x},t) = 1\,, \tag{3}$$

where $h_\alpha(\boldsymbol{\phi})$ is an interpolation function of the individual phases and $c_{\alpha,i}(\boldsymbol{x},t)$ is the concentration of an individual phase with respect to the corresponding component (Eiken et al., 2006). Eq. (2) subjects the phase composition c_i of the coexisting phases to the local mass conservation condition. Using the free energy functional for modeling the total energy of a heterogeneous system (Amos et al., 2018; Mittnacht et al., 2021; Schoof et al., 2020)

$$F(\boldsymbol{\phi},\boldsymbol{c},T) = \overline{F}^{\mathrm{int}}(\boldsymbol{\phi},\boldsymbol{\nabla\phi}) + \overline{F}^{\mathrm{chem}}(\boldsymbol{\phi},\boldsymbol{c},T) = \int_{\mathrm{V}} \left[\overline{f}^{\mathrm{int}}(\boldsymbol{\phi},\boldsymbol{\nabla\phi}) + \overline{f}^{\mathrm{chem}}(\boldsymbol{\phi},\boldsymbol{c},T)\right] \mathrm{dV}\,, \tag{4}$$

where $\overline{F}^{\mathrm{int}}$ and $\overline{F}^{\mathrm{chem}}$ are the diffuse interface and chemical energy contributions while $\overline{f}^{\mathrm{int}}$ and $\overline{f}^{\mathrm{chem}}$ are the diffuse interface and chemical energy density contributions, respectively, to the free energy potential. The former is a function of phase field variables $\boldsymbol{\phi}$ and its gradient $\boldsymbol{\nabla\phi}$ while the latter depends on phase field variable $\boldsymbol{\phi}$, composition field variables $\boldsymbol{c}$, and temperature T. The diffuse interface density contribution $\overline{f}^{\mathrm{int}}$ is computed as

$$\overline{f}^{\mathrm{int}}(\boldsymbol{\phi},\boldsymbol{\nabla\phi}) = \epsilon a(\boldsymbol{\phi},\boldsymbol{\nabla\phi}) + \frac{1}{\epsilon}\omega(\boldsymbol{\phi})\,, \tag{5}$$

where ϵ is a factor related to the length scale of the interface thickness, and $a(\boldsymbol{\phi},\boldsymbol{\nabla\phi})$ and $\omega(\boldsymbol{\phi})$ represent the gradient energy density and multi obstacle potential, respectively, described as (Nestler et al., 2005)

$$a(\boldsymbol{\phi},\boldsymbol{\nabla\phi}) = \sum_{\alpha=1}^{N}\sum_{\beta=1,\beta>\alpha}^{N} \Gamma_{\alpha\beta}\left[a_{\alpha\beta}(\boldsymbol{q}_{\alpha\beta})\right]|\boldsymbol{q}_{\alpha\beta}|^2, \qquad \text{with} \quad \boldsymbol{q}_{\alpha\beta} = \phi_\alpha\nabla\phi_\beta - \phi_\beta\nabla\phi_\alpha, \tag{6}$$

$$\omega(\boldsymbol{\phi}) = \begin{cases} \frac{16}{\pi^2}\sum_{\alpha=1}^{N}\sum_{\beta=1,\beta>\alpha}^{N}\Gamma_{\alpha\beta}\phi_\alpha\phi_\beta, & \text{if} \quad \phi_\alpha,\phi_\beta > 0 \quad \text{and} \quad \phi_\alpha+\phi_\beta = 1\,, \\ \infty, & \text{otherwise}\,. \end{cases} \tag{7}$$

Here $\boldsymbol{q}_{\alpha\beta}$ is the generalized antisymmetric gradient vector according to Nestler et al. (2005), $a_{\alpha\beta}(\boldsymbol{q}_{\alpha\beta})$ describes the anisotropy and $\Gamma_{\alpha\beta}$ is the interfacial energy density. Defining the chemical contribution $\overline{f}^{\mathrm{chem}}$ by using an interpolation function[2] $h_\alpha(\boldsymbol{\phi})$

$$\overline{f}^{\mathrm{chem}}(\boldsymbol{\phi},\boldsymbol{c},T) = \sum_{\alpha=1}^{N} f_\alpha^{\mathrm{chem}}(\boldsymbol{c}_\alpha,T) h_\alpha(\boldsymbol{\phi})\,, \tag{8}$$

where $f_\alpha^{\mathrm{chem}}(\boldsymbol{c}_\alpha,T)$ is the chemical free energy density of the phase α.

2.2. Incorporation of mechanical energy contribution

To include the effect of local strain $\boldsymbol{\epsilon} = \frac{1}{2}\left[\boldsymbol{\nabla u} + [\boldsymbol{\nabla u}]^{\mathrm{T}}\right]$ representing the symmetric part of the displacement gradient $\boldsymbol{\nabla u}$, where $\boldsymbol{u}$ is the displacement vector, we use an extended multiphase field model to include a total strain energy term $\overline{F}^{\mathrm{el}}(\boldsymbol{\phi},\boldsymbol{\varepsilon})$ in the free energy functional F, as per Schneider et al. (2018), Amos et al. (2018), and Schoof et al. (2020)

$$F(\boldsymbol{\phi},\boldsymbol{\varepsilon},\boldsymbol{c},T) = \int_{\mathrm{V}} \left[\overline{f}^{\mathrm{int}}(\boldsymbol{\phi},\boldsymbol{\nabla\phi}) + \overline{f}^{\mathrm{chem}}(\boldsymbol{\phi},\boldsymbol{c},T) + \overline{f}^{\mathrm{el}}(\boldsymbol{\phi},\boldsymbol{\varepsilon})\right] \mathrm{dV}\,. \tag{9}$$

Similar to Eq. (8), the interpolation function $h_\alpha(\boldsymbol{\phi})$ is used to determine the elastic strain energy density $\overline{f}^{\mathrm{el}}$ as

$$\overline{f}^{\mathrm{el}}(\boldsymbol{\phi},\boldsymbol{\varepsilon}) = \sum_{\alpha=1}^{N} f_\alpha^{\mathrm{el}}(\boldsymbol{\varepsilon}_\alpha) h_\alpha(\boldsymbol{\phi}) \quad \text{with} \tag{10}$$

$$f_\alpha^{\mathrm{el}}(\boldsymbol{\varepsilon}_\alpha) = \frac{1}{2}\left[\left[\boldsymbol{\varepsilon}_\alpha - \tilde{\boldsymbol{\varepsilon}}_\alpha\right]\cdot\boldsymbol{C}_\alpha\left[\boldsymbol{\varepsilon}_\alpha - \tilde{\boldsymbol{\varepsilon}}_\alpha\right]\right]\,, \tag{11}$$

where $\boldsymbol{\varepsilon}_\alpha$ is the phase specific strain with corresponding non elastic strain $\tilde{\boldsymbol{\varepsilon}}_\alpha$ according to the volumetric decomposition $\boldsymbol{\varepsilon} = \sum_\alpha \boldsymbol{\varepsilon}_\alpha h_\alpha(\boldsymbol{\phi})$ and $\boldsymbol{C}_\alpha$ is the phase specific stiffness tensor. The non elastic strain $\tilde{\boldsymbol{\varepsilon}}_\alpha$ contains eigenstrain $\boldsymbol{\varepsilon}_\alpha^0$, plastic strain $\boldsymbol{\varepsilon}_\alpha^{\mathrm{pl}}$, a concentration or temperature dependent eigenstrain $(\boldsymbol{\varepsilon}^0(\boldsymbol{c})_\alpha$ or $\boldsymbol{\varepsilon}^0(T)_\alpha)$

$$\tilde{\boldsymbol{\varepsilon}}_\alpha = \boldsymbol{\varepsilon}_\alpha^0 + \boldsymbol{\varepsilon}_\alpha^{\mathrm{pl}} + \boldsymbol{\varepsilon}_\alpha^0(\boldsymbol{c}) + \boldsymbol{\varepsilon}_\alpha^0(T)\,. \tag{12}$$

[2] Interpolation functions $h_\alpha(\boldsymbol{\phi})$ used in multiphase-field context can differ. The reader is referred to Choudhury and Nestler (2012) and Schneider et al. (2018) for an in-depth analysis of various interpolation functions. In this work, the interpolation function is defined as $h_\alpha(\boldsymbol{\phi}) = \phi_\alpha$.

Here, the eigenstrain, also known as stress free transformation strain[3] (Schoof et al., 2020; Amos et al., 2018), is induced due to the differences in the crystal structure between the bulk phase and phase evolving in it during the process of phase transformation.

Based on the mechanical jump condition that spatially depends on the interface orientation, it is intended to transform stresses and strains to a basis that is fixed on the interface orientation and then compute the energy by using locally averaged variables (Schneider et al., 2018). To this end, using a scalar field $L(\boldsymbol{\phi}) = \sum_{\alpha<\beta} \phi_\alpha \phi_\beta$, a homogenized normal vector to account for the interface orientation $\boldsymbol{n}$ is determined (Schoof et al., 2020)

$$\boldsymbol{n} = \frac{\boldsymbol{\nabla} L(\boldsymbol{\phi})}{|\boldsymbol{\nabla} L(\boldsymbol{\phi})|} \,. \tag{13}$$

Similar to the volumetric decomposition of strains, the volumetric decomposition of stresses $\boldsymbol{\sigma} = \sum_\alpha \boldsymbol{\sigma}_\alpha h_\alpha(\boldsymbol{\phi})$ is also defined. Transforming stresses and strains into an orthonormal basis $\boldsymbol{B} = \{\boldsymbol{n}, \boldsymbol{t}, \boldsymbol{s}\}$ using the Voigt notation and followed by reordering to separate normal and tangential components leads to Schneider et al. (2015)

$$\begin{aligned}
\boldsymbol{\sigma}_\alpha^B &:= \{\underbrace{\sigma^{nn}, \sigma^{nt}, \sigma^{ns}}_{\boldsymbol{\sigma}^n}, \underbrace{\sigma_\alpha^{tt}, \sigma_\alpha^{ss}, \sigma_\alpha^{ts}}_{\boldsymbol{\sigma}_\alpha^t}\}^\mathsf{T} = \{\boldsymbol{\sigma}^n, \boldsymbol{\sigma}_\alpha^t\}^\mathsf{T} \,, \\
\boldsymbol{\varepsilon}_\alpha^B &:= \{\underbrace{\varepsilon_\alpha^{nn}, 2\varepsilon_\alpha^{nt}, 2\varepsilon_\alpha^{ns}}_{\boldsymbol{\varepsilon}_\alpha^n}, \underbrace{\varepsilon^{tt}, \varepsilon^{ss}, 2\varepsilon^{ts}}_{\boldsymbol{\varepsilon}^t}\}^\mathsf{T} = \{\boldsymbol{\varepsilon}_\alpha^n, \boldsymbol{\varepsilon}^t\}^\mathsf{T} \,.
\end{aligned} \tag{14}$$

For an infinitesimal deformation on a singular plane, the jump of the variables $\boldsymbol{\sigma}^n$ and $\boldsymbol{\varepsilon}^t$ vanishes due to the force balance $[\![\boldsymbol{\sigma}^n]\!] = \boldsymbol{0}$ and the Hadamard kinematic compatibility condition $[\![\boldsymbol{\varepsilon}^t]\!] = \boldsymbol{0}$ (Silhavy, 2013). The discontinuous, phase dependent, contribution of stresses and strains thus remains

$$\boldsymbol{\sigma}_\alpha^t := \{\sigma_\alpha^{tt}, \sigma_\alpha^{ss}, \sigma_\alpha^{ts}\} \,, \tag{15}$$

$$\boldsymbol{\epsilon}_\alpha^n := \{\epsilon_\alpha^{nn}, 2\epsilon_\alpha^{nt}, 2\epsilon_\alpha^{ns}\}, \tag{16}$$

respectively. Similarly, the stiffness tensor for the α phase $\boldsymbol{C}_\alpha^B$ is also formulated in orthonormal basis $\boldsymbol{B}$ and in Voigt notation as

$$\boldsymbol{C}_\alpha^B = \left[\begin{array}{ccc|ccc}
C_\alpha^{nnnn} & C_\alpha^{nnnt} & C_\alpha^{nnns} & C_\alpha^{nntt} & C_\alpha^{nnss} & C_\alpha^{nnts} \\
C_\alpha^{ntnn} & C_\alpha^{ntnt} & C_\alpha^{ntns} & C_\alpha^{nttt} & C_\alpha^{ntss} & C_\alpha^{ntts} \\
C_\alpha^{nsnn} & C_\alpha^{nsnt} & C_\alpha^{nsns} & C_\alpha^{nstt} & C_\alpha^{nsss} & C_\alpha^{nsts} \\
\hline
C_\alpha^{ttnn} & C_\alpha^{ttnt} & C_\alpha^{ttns} & C_\alpha^{tttt} & C_\alpha^{ttss} & C_\alpha^{ttts} \\
C_\alpha^{ssnn} & C_\alpha^{ssnt} & C_\alpha^{ssns} & C_\alpha^{sstt} & C_\alpha^{ssss} & C_\alpha^{ssts} \\
C_\alpha^{tsnn} & C_\alpha^{tsnt} & C_\alpha^{tsns} & C_\alpha^{tstt} & C_\alpha^{tsss} & C_\alpha^{tsts}
\end{array}\right] = \begin{bmatrix} \boldsymbol{C}_\alpha^{nn} & \boldsymbol{C}_\alpha^{nt} \\ \boldsymbol{C}_\alpha^{tn} & \boldsymbol{C}_\alpha^{tt} \end{bmatrix} \,. \tag{17}$$

Here $\boldsymbol{C}_\alpha^{nn}$ and $\boldsymbol{C}_\alpha^{tt}$ are 3×3 symmetric matrices and $\boldsymbol{C}_\alpha^{nt}$ and $\boldsymbol{C}_\alpha^{tn}$ are 3×3 matrices for which the condition $\boldsymbol{C}_\alpha^{nt} = \left[\boldsymbol{C}_\alpha^{tn}\right]^\mathsf{T}$ is fulfilled. In a similar way, we introduce a proportionality matrix $\tilde{\boldsymbol{\tau}}$, later to be used for the computation of the elastic potential $P(\boldsymbol{\sigma}^n, \boldsymbol{\epsilon}^t, \boldsymbol{\phi})$, as

$$\tilde{\boldsymbol{\tau}} = \begin{bmatrix} \tilde{\boldsymbol{\tau}}^{nn} & \tilde{\boldsymbol{\tau}}^{nt} \\ \tilde{\boldsymbol{\tau}}^{tn} & \tilde{\boldsymbol{\tau}}^{tt} \end{bmatrix} \,, \tag{18}$$

where each entity is given as

$$\tilde{\boldsymbol{\tau}}^{nn} = \sum_\alpha \boldsymbol{\tau}_\alpha^{nn} h_\alpha(\boldsymbol{\phi}) := -\sum_\alpha [\boldsymbol{C}_\alpha^{nn}]^{-1} \phi_\alpha \,, \tag{19}$$

$$\tilde{\boldsymbol{\tau}}^{nt} = \sum_\alpha \boldsymbol{\tau}_\alpha^{nt} h_\alpha(\boldsymbol{\phi}) := \sum_\alpha [\boldsymbol{C}_\alpha^{nn}]^{-1} \boldsymbol{C}_\alpha^{nt} \phi_\alpha \,, \tag{20}$$

$$\tilde{\boldsymbol{\tau}}^{tt} = \sum_\alpha \boldsymbol{\tau}_\alpha^{tt} h_\alpha(\boldsymbol{\phi}) := -\sum_\alpha \left[\boldsymbol{C}_\alpha^{tt} - \boldsymbol{C}_\alpha^{tn} [\boldsymbol{C}_\alpha^{nn}]^{-1} \boldsymbol{C}_\alpha^{nt}\right] \phi_\alpha \,. \tag{21}$$

Using the defined notations, the strain energy density in Eq. (11) can be reformulated for the α phase as a sum of scalar products in the previously defined orthonormal basis $\boldsymbol{B}$ as

$$\begin{aligned}
f_\alpha^{\mathrm{el}}(\boldsymbol{\varepsilon}_\alpha^B) = \frac{1}{2} \Big[& [\boldsymbol{\varepsilon}_\alpha^n - \tilde{\boldsymbol{\varepsilon}}_\alpha^n] \cdot \boldsymbol{C}_\alpha^{nn} [\boldsymbol{\varepsilon}_\alpha^n - \tilde{\boldsymbol{\varepsilon}}_\alpha^n] \\
& + [\boldsymbol{\varepsilon}_\alpha^n - \tilde{\boldsymbol{\varepsilon}}_\alpha^n] \cdot \boldsymbol{C}_\alpha^{nt} [\boldsymbol{\varepsilon}_\alpha^t - \tilde{\boldsymbol{\varepsilon}}_\alpha^t] \\
& + [\boldsymbol{\varepsilon}_\alpha^t - \tilde{\boldsymbol{\varepsilon}}_\alpha^t] \cdot \boldsymbol{C}_\alpha^{tn} [\boldsymbol{\varepsilon}_\alpha^n - \tilde{\boldsymbol{\varepsilon}}_\alpha^n] \\
& + [\boldsymbol{\varepsilon}_\alpha^t - \tilde{\boldsymbol{\varepsilon}}_\alpha^t] \cdot \boldsymbol{C}_\alpha^{tt} [\boldsymbol{\varepsilon}_\alpha^t - \tilde{\boldsymbol{\varepsilon}}_\alpha^t] \Big] \,.
\end{aligned} \tag{22}$$

[3] Since the strain is induced despite the absence of external deformation (or stress).

2.3. Evolution equations

From the free energy functionals in Eq. (9), a set of evolution equations for the phase fields ϕ_α, the concentrations $\boldsymbol{c}_i$ and the strain field $\boldsymbol{\epsilon}$ defined by the displacement vector $\boldsymbol{u}$ can be derived by variational differentiation. Details of the derivations are given in Nestler et al. (2005) and Steinbach et al. (1996). The resulting equations are called Cahn Hilliard and Allen Cahn equations and need to be solved to obtain the evolution of the composition and phase fields. The Allen Cahn equation is formulated as (Amos et al., 2018; Steinbach and Pezzolla, 1999; Steinbach, 2009)

$$\frac{\partial \phi_\alpha}{\partial t} = -\frac{1}{\epsilon \tilde{N}} \sum_{\beta \neq \alpha}^{\tilde{N}} M_{\alpha\beta} \left[\frac{\delta \overline{F}^{\text{int}}}{\delta \phi_\alpha} - \frac{\delta \overline{F}^{\text{int}}}{\delta \phi_\beta} + \frac{8\sqrt{\phi_\alpha \phi_\beta}}{\pi} \left[\Delta^{\text{chem}}_{\alpha\beta} + \Delta^{\text{el}}_{\alpha\beta} \right] \right], \tag{23}$$

where $\tilde{N}$ is the number of locally active phases such that $\tilde{N} \leq N$, $\Delta^{\text{chem}}_{\alpha\beta}(\boldsymbol{c}, T, \boldsymbol{\phi})$ and $\Delta^{\text{el}}_{\alpha\beta}(\boldsymbol{\sigma}^n, \boldsymbol{\epsilon}^t, \boldsymbol{\phi})$ are chemical and elastic driving forces, respectively, given by

$$\begin{aligned} \Delta^{\text{chem}}_{\alpha\beta}(\boldsymbol{c}, T, \boldsymbol{\phi}) &= \left[\frac{\delta}{\delta \phi_\beta} - \frac{\delta}{\delta \phi_\alpha} \right] \overline{F}^{\text{chem}}, \\ \Delta^{\text{el}}_{\alpha\beta}(\boldsymbol{\sigma}^n, \boldsymbol{\epsilon}^t, \boldsymbol{\phi}) &= \left[\frac{\delta}{\delta \phi_\beta} - \frac{\delta}{\delta \phi_\alpha} \right] \overline{F}^{\text{el}}. \end{aligned} \tag{24}$$

The variational derivation of Eq. (9) with respect to ϕ_α can be computed as

$$\frac{\delta F}{\delta \phi_\alpha} = \left[\frac{\partial}{\partial \phi_\alpha} - \nabla \cdot \frac{\partial}{\partial \phi_\alpha} \right] \overline{f}^{\text{x}}, \tag{25}$$

where $\overline{f}^{\text{x}}$ are the interfacial, chemical, and elastic density contributions. The final form of $\Delta^{\text{chem}}_{\alpha\beta}$ is well known (see e.g. Amos et al. (2018) and Raza and Klusemann (2020)). For the elastic free energy density, we consider the Legendre transform that gives an overall elastic potential $P(\boldsymbol{\sigma}^n, \boldsymbol{\epsilon}^t, \boldsymbol{\phi})$ based on continuous variables. The driving force thus becomes (Schoof et al., 2020)

$$\Delta^{\text{el}}_{\alpha\beta}(\boldsymbol{\sigma}^n, \boldsymbol{\epsilon}^t, \boldsymbol{\phi}) = \frac{\partial P(\boldsymbol{\sigma}^n, \boldsymbol{\epsilon}^t, \boldsymbol{\phi})}{\partial \phi_\beta} - \frac{\partial P(\boldsymbol{\sigma}^n, \boldsymbol{\epsilon}^t, \boldsymbol{\phi})}{\partial \phi_\alpha}, \tag{26}$$

where the overall elastic potential $P(\boldsymbol{\sigma}^n, \boldsymbol{\epsilon}^t, \boldsymbol{\phi})$ is determined via

$$P(\boldsymbol{\sigma}^n, \boldsymbol{\epsilon}^t, \boldsymbol{\phi}) = \left[\begin{bmatrix} \boldsymbol{\sigma}^n \\ \boldsymbol{\epsilon}^t \end{bmatrix} \cdot \tilde{\boldsymbol{\tau}} \begin{bmatrix} \boldsymbol{\sigma}^n \\ \boldsymbol{\epsilon}^t \end{bmatrix} - \sum_\alpha \left[\begin{bmatrix} \boldsymbol{\sigma}^n \\ \boldsymbol{\epsilon}^t \end{bmatrix} \cdot \begin{bmatrix} \boldsymbol{I} & \boldsymbol{\tau}^{nt}_\alpha \\ \boldsymbol{0} & \boldsymbol{\tau}^{tt}_\alpha \end{bmatrix} \begin{bmatrix} \tilde{\boldsymbol{\epsilon}}^n_\alpha \\ \tilde{\boldsymbol{\epsilon}}^t_\alpha \end{bmatrix} \right] + \frac{1}{2} \sum_\alpha \left[\tilde{\boldsymbol{\epsilon}}^t_\alpha \cdot \boldsymbol{\tau}^{nn}_\alpha \tilde{\boldsymbol{\epsilon}}^t_\alpha \right] \right] h_\alpha(\boldsymbol{\phi}), \tag{27}$$

where $\boldsymbol{I}$ and $\boldsymbol{0}$ are second order identity and zero tensors. Defining the normal and tangential components of interpolated stress free (eigen)strain $\boldsymbol{\epsilon}^{0,n}_\alpha$ and $\boldsymbol{\epsilon}^{0,t}_\alpha$ as

$$\boldsymbol{\epsilon}^{0,n}_\alpha = \sum_\alpha [\tilde{\boldsymbol{\epsilon}}^n_\alpha + \boldsymbol{\tau}^{nt}_\alpha \tilde{\boldsymbol{\epsilon}}^t_\alpha] h_\alpha(\boldsymbol{\phi}) \tag{28}$$

$$\boldsymbol{\epsilon}^{0,t}_\alpha = \sum_\alpha \boldsymbol{\tau}^{tt}_\alpha \tilde{\boldsymbol{\epsilon}}^t_\alpha h_\alpha(\boldsymbol{\phi}), \tag{29}$$

and using the proportionality matrix $\tilde{\boldsymbol{\tau}}$, the stress $\overline{\boldsymbol{\sigma}}^B$ is computed as (Schneider et al., 2018)

$$\overline{\boldsymbol{\sigma}}^B = \begin{bmatrix} -[\tilde{\boldsymbol{\tau}}^{nn}]^{-1} & -[\tilde{\boldsymbol{\tau}}^{nn}]^{-1} \tilde{\boldsymbol{\tau}}^{nt} \\ -\tilde{\boldsymbol{\tau}}^{tn} [\tilde{\boldsymbol{\tau}}^{nn}]^{-1} & -\tilde{\boldsymbol{\tau}}^{tt} - \tilde{\boldsymbol{\tau}}^{tn} [\tilde{\boldsymbol{\tau}}^{nn}]^{-1} \tilde{\boldsymbol{\tau}}^{nt} \end{bmatrix} \begin{bmatrix} \boldsymbol{\epsilon}^n \\ \boldsymbol{\epsilon}^t \end{bmatrix} + \begin{bmatrix} [\tilde{\boldsymbol{\tau}}^{nn}]^{-1} & \boldsymbol{0} \\ -\tilde{\boldsymbol{\tau}}^{tn} [\tilde{\boldsymbol{\tau}}^{nn}]^{-1} & -\boldsymbol{I} \end{bmatrix} \begin{bmatrix} \boldsymbol{\epsilon}^{0,n}_\alpha \\ \boldsymbol{\epsilon}^{0,t}_\alpha \end{bmatrix}. \tag{30}$$

The evolution equation for each $K-1$ independent concentration variables c_i (Eq. (2)) is defined by the gradient of chemical potential $\boldsymbol{\mu} = \dfrac{\partial \overline{f}^{\text{chem}}}{\partial \boldsymbol{c}}$, being a tuple of $\boldsymbol{\mu} = \{\mu_0, \dots, \mu_i, \dots, \mu_{k-1}\}$ yields

$$\frac{\partial c_i}{\partial t} = \nabla \cdot \left[\sum_{j=1}^{K-1} M_{ij}(\boldsymbol{\phi}) \nabla \mu_j \right], \tag{31}$$

where $M_{ij}(\boldsymbol{\phi})$ is the mobility of the interface. The individual phase mobilities are interpolated as

$$M_{ij}(\boldsymbol{\phi}) = \sum_{\alpha=1}^{N-1} M_{\alpha,ij} h_\alpha(\boldsymbol{\phi}) \quad \text{with} \quad M_{\alpha,ij} = D_{\alpha,ij} \frac{\partial c_{\alpha,i}(\boldsymbol{\mu}, T)}{\partial \mu_j}. \tag{32}$$

Here $D_{\alpha,i,j}$ are the interdiffusivities for each phase α. Decomposing the interdiffusivities additively into two contributions: volume and grain boundary, we introduce a third order tensor $\boldsymbol{D}$ as

$$\boldsymbol{D} = \boldsymbol{D}^{\text{vol}} + \boldsymbol{D}^{\text{gb}}, \tag{33}$$

where $\boldsymbol{D}^{\text{vol}}$ and $\boldsymbol{D}^{\text{gb}}$ represent the contributions of volume and grain boundary, leading to the definition of the following symmetric diffusion matrix for each component (Hötzer et al., 2019)

$$\boldsymbol{D}_i = \begin{bmatrix} D_{i,1,1} & D_{i,2,1} & \cdots & D_{i,N-1,1} & D_{i,N,1} \\ & D_{i,2,2} & \ddots & \vdots & \vdots \\ & & \ddots & D_{i,N-1,N-2} & \vdots \\ & & & D_{i,N-1,N-1} & D_{i,N,N-1} \\ & & & & D_{i,N,N} \end{bmatrix}, \tag{34}$$

where blue colored contributions denote volume diffusion, while green colored grain boundary diffusion.

Note that the evolution Eqs. (23) and (31) require the computation of the equilibrium chemical potential $\boldsymbol{\mu}$. Choudhury and Nestler (2012) presented an implicit and explicit scheme for the derivation. In this work, we pursue an implicit scheme derived from the constraint in Eq. (2) for the calculation of $K-1$ independent components μ_i by simultaneously solving the $K-1$ constraints for each of the $K-1$ independent concentration variables $\boldsymbol{c}_i$ using Newton Raphson scheme according to (Eiken et al., 2006)

$$\frac{\partial \mu_i}{\partial t} = \left[\sum_{\alpha=1}^{N} h_\alpha(\boldsymbol{\phi}) \frac{\partial c_{\alpha,i}(\boldsymbol{\mu},T)}{\partial \mu_j}\right]^{-1}_{ij} \left[\nabla \cdot \left[\sum_{j=1}^{K-1} M_{ij}(\boldsymbol{\phi}) \nabla \mu_j\right] - \sum_{\alpha=1}^{N} c_{\alpha,i}(\boldsymbol{\mu},T) \frac{\partial h_\alpha(\boldsymbol{\phi})}{\partial t}\right]. \tag{35}$$

Here the thermodynamic variable $\boldsymbol{\mu}$ related to phase concentration $c_{\alpha,i}$ is directly solved instead of explicitly solving for phase concentrations $c_{\alpha,i}$, since concentrations $c_{\alpha,i}(\boldsymbol{\mu},T)$ are defined as functions of the thermodynamic variable $\boldsymbol{\mu}$ (Choudhury and Nestler, 2012).

Finally, for evolution of displacements $\boldsymbol{u}$, we solve the static momentum balance equation

$$\boldsymbol{\nabla} \cdot \boldsymbol{\sigma} = \boldsymbol{0}, \tag{36}$$

where $[\boldsymbol{\nabla} \cdot \boldsymbol{\sigma}]_i = \dfrac{\partial \sigma_{ij}}{\partial x_j}$ is the divergence of stress tensor. Based on the mechanical equilibrium condition, the dynamic variables associated with the elastic energy contribution are evaluated and solved within the chemo elastic model framework used in this work.

2.4. Parameters of the multiphase field model

The parameters required to implement the multiphase field framework are chemical free energy of each component α, F_α^{chem}, gradient energy density, $a_{\alpha\beta}$, interfacial energy density, $\Gamma_{\alpha\beta}$, mobility between dually interacting phases, M_{ij}, and diffusion matrix, $\boldsymbol{D}_i$.

According to the binary phase diagram of an Al Mg system (Handbook, 1992; Liu et al., 2014), thermodynamically the formation of Al_3Mg_2 (β phase) and $Al_{12}Mg_{17}$ (γ phase) is expected at temperatures under 450 °C, also generally observed in the solid state joining of Al Mg, see e.g., Suhuddin et al. (2014), Jafarian et al. (2016), AFGHAHI et al. (2016) and Panteli et al. (2012). Depending on the considered composition of the alloy, particular volume fractions of the different solid phases are established. Since the Al_3Mg_2 intermetallic phase is a stoichiometric compound, the free energy composition plot represents a single point instead of a parabola. To ensure Al_3Mg_2 evolution in the Al matrix, the values for the parabolic curve for Al_3Mg_2 must be assumed. The "latus rectum" of the parabola dictates the final thickness of Al_3Mg_2 in Al. Since the latus rectum is assumed, this also implies an assumption of the obtained thickness of the Al_3Mg_2. To avoid assumptions that strongly influence the final thickness, Al_3Mg_2 is not considered further in this work. Additionally, including the Al_3Mg_2 stoichiometric compound would require using a smaller time step, which adversely impacts the computational time. For the sake of implementing the current model that involves mechanical driving forces in addition to the chemical, we only consider the evolution of the non stoichiometric $Al_{12}Mg_{17}$ intermetallic compound in the Mg matrix for which an analytical chemical free energy density function is available. Thus an accurate parabolic description is used to obtain results unaffected by the strong assumptions.

To obtain the free energy F_α^{chem} consistent with the phase equilibrium diagram, the CALPHAD method is used for the thermodynamic assessment of the Al Mg system (Zhong et al., 2005; Murray, 1982; Saunders, 1990; Zuo and Chang, 1993). To this end, assuming a constant molar volume fraction V_{m} for simplicity, the chemical free energy density of various components of the Al Mg system is extracted using Thermo Calc and subsequently approximated according to the approach in Amos et al. (2018) as parabolic functions. Suhuddin et al. (2013) measured experimentally thermal cycles during refill FSSW of dissimilar Al Mg sheets and observed maximum temperatures at the weld interface in the range of 370 °C 450 °C. Based on the process simulation of the refill FSSW process in Section 4.1, this result is confirmed, therefore, the Gibbs free energy potential of all phases with respect to Mg concentration is computed at 450 °C, see Fig. 2.[4] The equilibrium phase compositions can thus be extracted and are summarized in Table 1.

In an Al Mg system, the $Al_{12}Mg_{17}$ intermetallic phase has a bcc structure while the Mg matrix phase has an hcp crystal structure (Han et al., 2015; Luo et al., 2012). These crystal structure differences in phases yield misfitting of corresponding elementary cells of those phases, eventually resulting in eigenstrains. Using the one coordinate system shown by Han et al. (2015),

[4] Note that in the previous work of the authors (Raza and Klusemann, 2020), chemical-free energy was computed at 400 °C, in the unit of J mol^{-1}, whereas in the present work, based on the performed process simulation, it is computed at 450 °C in the unit of J m^{-3}.

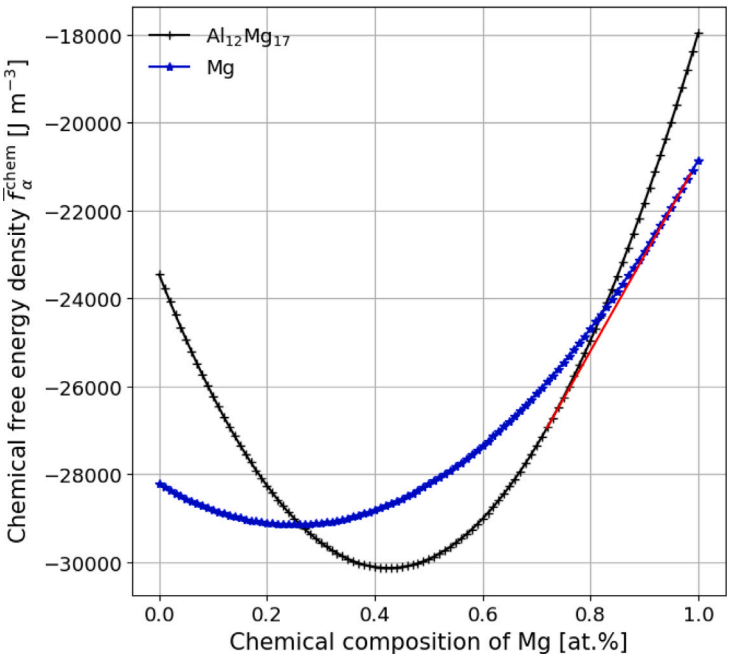

Fig. 2. Gibbs free energy density of $Al_{12}Mg_{17}$ and Mg phases with respect to the composition of Mg, where the common tangent is shown in red. Quantitative thermodynamic data is obtained via Thermo-Calc to construct the energy curves accordingly.

Table 1
Equilibrium phase compositions (in mole fraction) with respect to the Mg concentration in the system at $T = 450$ °C.

Phases	Equilibrium phase composition
${}^{e}c_{\gamma}$	0.719
${}^{e}c_{Mg}$	0.986

enables setting x , y , and z axis as $[11\bar{2}0]_\alpha$, $[\bar{1}100]_\alpha$, and $[0001]_\alpha$, respectively. In Fig. 3, the lattice misorientations and corresponding crystal structures are depicted in a x y plane. The lattice deformation matrix resulting from the change of matrix lattice into precipitate lattice is given as (Han et al., 2015)

$$\begin{bmatrix} \frac{a_\gamma\sqrt{3}-6a_\alpha}{6a_\alpha} & 0 & 0 \\ 0 & \frac{a_\gamma\sqrt{11}-6\sqrt{3}a_\alpha}{6\sqrt{3}a_\alpha} & 0 \\ 0 & 0 & \frac{a_\gamma\sqrt{2}-3c_\alpha}{3c_\alpha} \end{bmatrix}, \tag{37}$$

where a_α and c_α are the lattice parameters of the Mg with hcp structure; a_γ is the lattice parameter of the $Al_{12}Mg_{17}$ phase with bcc structure. Defining Θ as the lattice rotation, the eigenstrain tensor matrix of the precipitation transformation matrix is obtained using the rotational transformation of the lattice deformation matrix as

$$\epsilon_{ij}^{0} = [R(\Theta)]^{\mathsf{T}} \begin{bmatrix} \frac{a_\gamma\sqrt{3}-6a_\alpha}{6a_\alpha} & 0 & 0 \\ 0 & \frac{a_\gamma\sqrt{11}-6\sqrt{3}a_\alpha}{6\sqrt{3}a_\alpha} & 0 \\ 0 & 0 & \frac{a_\gamma\sqrt{2}-3c_\alpha}{3c_\alpha} \end{bmatrix} [R(\Theta)], \tag{38}$$

and $R(\Theta)$ is the orientation mismatch defined as

$$R(\Theta) = \begin{bmatrix} \cos\Theta & \sin\Theta & 0 \\ -\sin\Theta & \cos\Theta & 0 \\ 0 & 0 & 1 \end{bmatrix}. \tag{39}$$

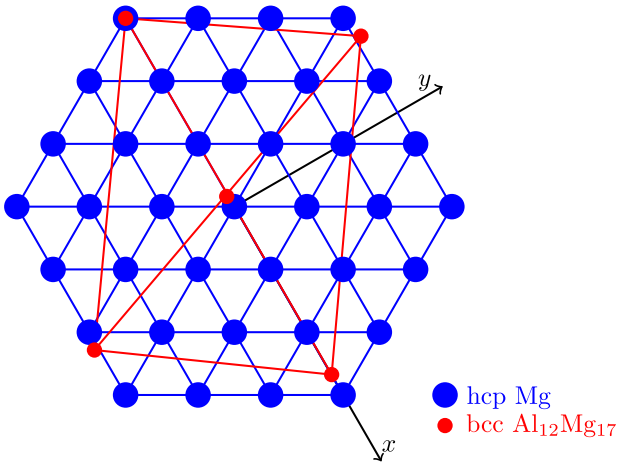

Fig. 3. Schematic illustration of the lattice transformation from hcp Mg matrix to bcc $Al_{12}Mg_{17}$ intermetallic phase.

The parameters a_α, c_α, a_γ, and Θ are given in Table 4.

It is well known that the interface energies and mobilities are difficult to determine experimentally or computationally (Park and Arróyave, 2009); hence, we assume the values of interface energies in this work and consider these as simulation parameters while taking the values of mobilities from the previous work of the authors (Raza and Klusemann, 2020) using the expression given in Kim et al. (2009). All the material parameters are summarized in Table 4. For the sake of simplicity and computational efficiency, Eqs. (37) (39) are reduced to 2×2 matrices since the domain for the phase field simulations is considered two dimensional in this work.

3. Simulation setup

3.1. Finite element model

A finite element model according to the refill FSSW experimental setup (Suhuddin et al., 2014) is pursued in DEFORM3D, which is well suited for simulating metal forming processes, using an updated Lagrangian formulation in combination with automatic remeshing (He et al., 2014). A thermo mechanical model comprising of rigid viscoplastic material model and a heat transfer model that considers the heat generation due to friction and plastic deformation is implemented. To this end, we model the pin, sleeve, and clamping ring as rigid bodies with the dimensions shown in Fig. 4 while the workpieces, i.e., the two sheets, are modeled as rigid viscoplastic. The two sheets, namely AA5754 (top) and AZ31 (bottom) of thickness 2 mm, are modeled as temperature and strain rate dependent via the Johnson Cook material model according to

$$\sigma = [A + B\epsilon^n]\left[1 + H \ln \frac{\dot{\epsilon}}{\dot{\epsilon}_0}\right]\left[1 - T^{*m}\right], \tag{40}$$

with the homologous temperature

$$T^{*m} = \frac{T - T^0}{T^{\text{melt}} - T^0}. \tag{41}$$

In Eqs. (40) and (41), $\dot{\epsilon}_0$ is the reference strain rate, and T^0 and T^{melt} the room and melting temperature, respectively, A is the yield strength of the material at room temperature, B and n the hardening modulus and work hardening exponent, respectively, showing the impact of strain hardening, and H and m the strain rate hardening and thermal softening coefficient, respectively. The employed material properties for AA5754 and AZ31 are given in Table 2, denoted as Al and Mg, respectively.

Each stage of the refill FSSW process, i.e., plunging, dwelling, and retraction, takes time t^{stage} to complete. However, since the major strain is applied to the specimen during the first stage, only the plunging phase is considered in this work. During the plunging stage, the sleeve plunges h^{sleeve} distance in the top sheet, while the pin moves h^{pin} distance in the opposite direction, while both rotating with angular velocity $\omega^{\text{pin}} = \omega^{\text{sleeve}}$. The process parameters are given in Table 3.

To establish a contact condition between the rigid tool and Al sheet, and Al and Mg sheets, penalty contact algorithm along with a frictional condition via shear friction law is employed as per Jain et al. (2018), given as

$$\tau = f\tau^{\max}, \tag{42}$$

where τ is the contact shear stress, f the shear friction factor set as 0.4 and 0.12 for sleeve and workpiece, and pin and clamping ring, respectively, while $\tau^{\max}$ is the shear yield strength defined as 0.577 times the yield strength. Shear friction law is set to capture mechanical interaction between the tool and workpiece in the actual forming operation (Chen et al., 2020; Jain et al., 2018). Using

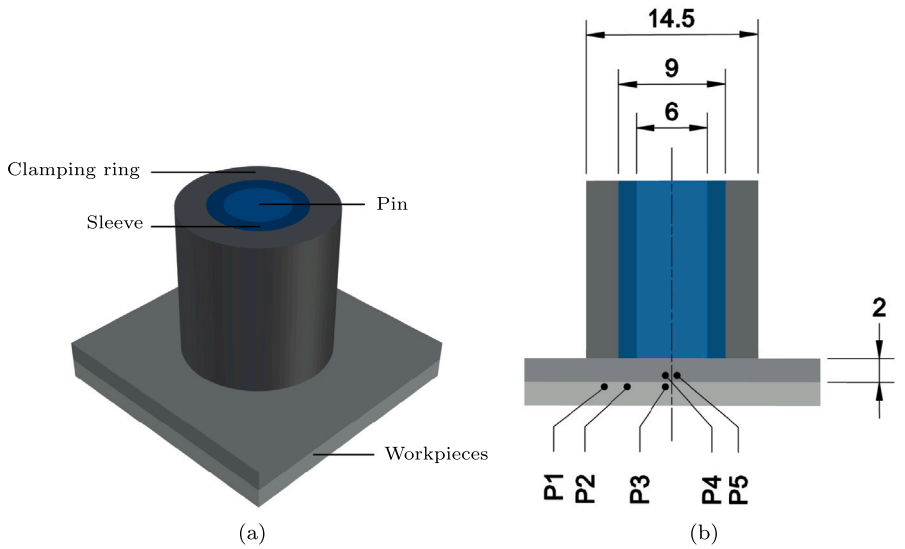

Fig. 4. Components of refill FSSW process modeled in DEFORM3D. The pin goes in the sleeve, which in turn goes in the clamping ring against the backing bar. The setup is placed on top of the workpiece, kept in place via the clamping ring. The workpiece on top is Al, while the bottom is Mg. Dimensions of the refill FSSW components are given in mm. Points 1–5 are the nodes evaluated during the simulation.

Table 2
Material parameters required for the finite-element model of the refill FSSW process. For Al and Mg, the material properties for AA5754 and AZ31 are taken from MatWeb, and the Johnson–Cook parameters are taken from literature.

Parameter	Symbol	Magnitude	Unit
Density of Al	ρ^{Al}	2.67×10^{-6}	kg mm^{-3}
Modulus of elasticity of Al	E^{Al}	70.3×10^{3}	MPa
Poissons ratio of Al	ν^{Al}	0.33	–
Coefficient of thermal expansion of Al	α^{Al}	2.39×10^{-7}	mm mm^{-1} K^{-1}
Thermal conductivity of Al	K^{Al}	125	N s^{-1} K^{-1}
Melting temperature of Al	$T^{melt,Al}$	600	°C
Yield strength for Al (Smerd, 2005)	A^{Al}	67.456	MPa
Hardening modulus for Al (Smerd, 2005)	B^{Al}	471.242	MPa
Strain rate hardening for Al (Smerd, 2005)	H^{Al}	0.002979	–
Work hardening exponent for Al (Smerd, 2005)	n^{Al}	0.4241	–
Thermal softening coefficient for Al[a]	m^{Al}	0.5186	–
Reference strain rate for Al (Smerd, 2005)	$\dot{\epsilon}_0^{Al}$	1	s^{-1}
Density of Mg	ρ^{Mg}	1.77×10^{-6}	kg mm^{-3}
Modulus of elasticity of Mg	E^{Mg}	17×10^{3}	MPa
Poissons ratio of Mg	ν^{Mg}	0.35	–
Coefficient of thermal expansion of Mg	α^{Mg}	2.6×10^{-7}	mm mm^{-1} K^{-1}
Thermal conductivity of Mg	K^{Mg}	96	N s^{-1} K^{-1}
Melting temperature of Mg	$T^{melt,Mg}$	605	°C
Yield strength for Mg (Abbassi et al., 2016)	A^{Mg}	172	MPa
Hardening modulus for Mg (Abbassi et al., 2016)	B^{Mg}	360.73	MPa
Strain rate hardening for Mg (Abbassi et al., 2016)	H^{Mg}	0.092	–
Work hardening exponent for Mg[a]	n^{Mg}	2.45	–
Thermal softening coefficient for Mg (Abbassi et al., 2016)	m^{Mg}	0.95	–
Reference strain rate for Mg (Abbassi et al., 2016)	$\dot{\epsilon}_0^{Mg}$	0.01	s^{-1}
Room Temperature	T^{0}	20	°C

[a]Note: Parameters are adjusted to fit the simulation results with the experiments.

Table 3
Process parameters required for the finite-element model of the refill FSSW process, based on the work of Suhuddin et al. (2013).

Parameter	Symbol	Magnitude	Unit
Plunging, dwelling, retracting time	t^{stage}	2	s
Sleeve travel	h^{sleeve}	1.6	mm
Pin travel	h^{pin}	2.0	mm
Pin and sleeve rotational speed	$\omega^{pin} = \omega^{sleeve}$	1900	rpm

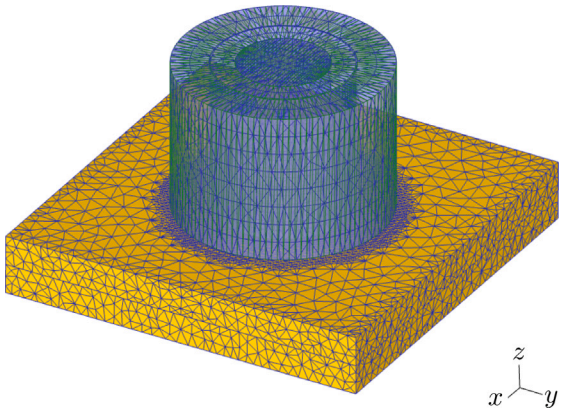

Fig. 5. The meshed refill FSSW model in DEFORM3D. The workpiece consists of 40 827 and 44 110 elements for the Al and Mg, respectively, 10 772 elements for the pin, 8775 elements for the sleeve, and 6488 elements for the clamping ring. The workpiece directly below the tool is meshed finer compared to the rest of the workpiece.

DEFORM3D recommended values for forming processes, heat transfer coefficient for conduction between the contact surfaces and convention between the contact surfaces as well as environment is set to 11 N s^{-1} mm^{-1} K^{-1} and 0.02 N s^{-1} mm^{-1} K^{-1}, respectively, while emissivity is assumed as 0.7 and 0.07 for Al and Mg respectively.

Fig. 5 shows the meshed model with 40 827 and 44 110 tetrahedral elements for the Al and Mg workpiece, respectively, 8775 for the sleeve, 10 772 for the pin, and 6488 for the clamping ring. Note that the area of the sheets under the tool is meshed finer as the region is expected to undergo severe deformation. Additionally, automatic remeshing feature of DEFORM3D via adaptive remeshing is used to tackle high mesh distortion especially at the process zone (Jain et al., 2018). The four side faces of each sheet and the bottom face of Mg sheet is fixed in all directions. The time step size in the simulation is set constant to 0.03 s.

During the simulation, Points 1 3 and Points 4 5 (illustrated in Fig. 4(b)) are evaluated to obtain strain and temperature results, respectively.

3.2. Multiphase field model

To predict the intermetallic compound evolution based on the multi phase field model described in Section 2, a two dimensional model is constructed in PACE3D (Parallel Algorithms for Crystal Evolution in 3D) (Hötzer et al., 2018) to simulate the temperature and strain driven diffusion during refill FSSW of Al and Mg. As previously mentioned, only the diffusion of γ $Al_{12}Mg_{17}$ into Mg matrix is considered. Besides using a computationally efficient parallelized code, non dimensionalizing the input parameters using an appropriate scheme ensures the accuracy of the simulations. During the initialization, some preconditioning steps are performed to facilitate convergence towards mechanical equilibrium (Amos et al., 2018). To this end, an initial microstructure with various $Al_{12}Mg_{17}$ crystal seeds is assumed, as shown in Fig. 6, where the bulk Mg matrix with $Al_{12}Mg_{17}$ grains of the intermetallic compound is illustrated. As an idealistic structure, we set the initial thickness of the $Al_{12}Mg_{17}$ layer to 0.6 μm (as per Raza and Klusemann, 2020) with a randomized grain size of 0.8 1.3 μm. Interfaces of $Al_{12}Mg_{17}$/Mg as well as the intermetallic compound grain boundaries are explicitly defined in the initial microstructure. To tackle the problem at hand, two components, i.e., $K = 2$, are defined to indicate Al and Mg. Eleven phase field variables are introduced to represent the Mg bulk phase with $\phi_1 = 1$ and randomly generated grains $\phi_i = 1$ for $i = 2, \dots, 11$ in order to create an initial structure with intermetallic grains. The boundary condition in terms of phase fields and concentration is set to be of Neumann type along the x axis and periodic type along the y axis for both purely chemical and chemo mechanical models. For strain, the left side is fixed with Dirichlet boundary condition while the right side is set as stress free and displacement type boundary condition for eigen and external strain, respectively. Periodicity along the y axis can be assumed since a small unit cell of a larger welding zone is simulated that could be strung together. A summary of the material parameters used in the current multiphase field model is given in Table 4.

Among many methods available to solve Eqs. (23), (31), (35), and (36), as reviewed by Bellemans et al. (2018), we use an explicit finite difference approach for two dimensional square lattices with uniform lattice spacing Δx. The discrete time step in such cases is typically set as (Qin and Bhadeshia, 2010)

$$\Delta t < \frac{1}{2}\frac{[\Delta x]^2}{D_{\max}}, \tag{43}$$

where $D_{\max}$ is the largest of all diffusivities in the present system.

The partial differential Eqs. (23) and (31) contain both derivatives in space and time, resulting in a need for discretization in both domains. The time evolution of a variable Ω, i.e., either the phase field variable ϕ or composition field variable c, is given by

$$\Omega(i,j,t+\Delta t) = \Omega(i,j,t) + \frac{\partial \Omega}{\partial t}(i,j,t)\Delta t\,. \tag{44}$$

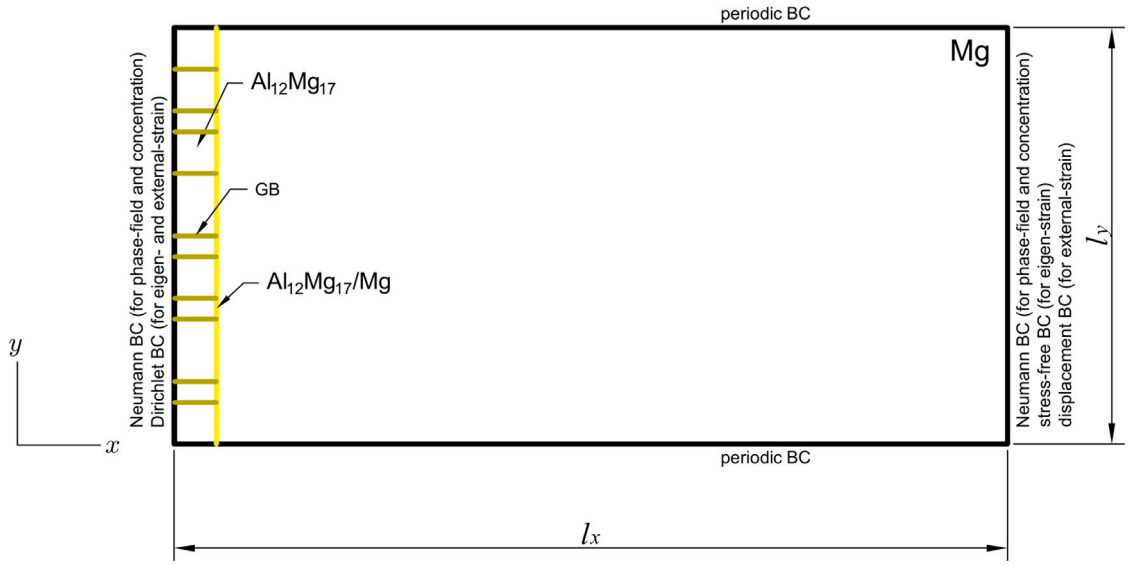

Fig. 6. Representation of the initial microstructure, consisting of Mg and several $Al_{12}Mg_{17}$ seeds. The $Al_{12}Mg_{17}$/Mg boundary (yellow) and $Al_{12}Mg_{17}$ grain boundaries (olive) are indicated in the initial microstructure. Diffusion rates are defined for the bulk Mg and $Al_{12}Mg_{17}$ along with the boundaries between $Al_{12}Mg_{17}$/Mg and intermetallic compound grain boundaries (GB).

Table 4
Material parameters used in the current multiphase-field model. Static diffusion rates are taken from Brennan et al. (2012). CALPHAD approach is used to obtain Gibbs energies at $T = 450$ °C. The mobility and diffusivity of the intermetallic compound grain boundaries is usually taken higher than that of the bulk regions (Hong and Huh, 2006; Kim et al., 2009), a similar approach is adopted in this work. Interface energies are selected as simulation parameters.

Parameter	Symbol	Magnitude	Unit
Working temperature	T	723	K
Lattice spacing	$\Delta x = \Delta y$	0.15	μm
Grid size	$l_x \times l_y$	30 × 15	μm × μm
Interface width	ξ_{ij}	$4\Delta x$	μm
Molar Volume	V_m	7.0×10^{-6}	$\mu m^3\ mol^{-1}$
Diffusion rate of Al (Brennan et al., 2012; Kulkarni and Luo, 2013)	D_{Al}	1.9×10^{-2}	$\mu m^2\ s^{-1}$
Diffusion rate of Mg (Brennan et al., 2012; Kulkarni and Luo, 2013)	D_{Mg}	4.9×10^{-3}	$\mu m^2\ s^{-1}$
Diffusion rate of $Al_{12}Mg_{17}$ (Brennan et al., 2012; Kulkarni and Luo, 2013)	D_γ	1.3×10^{-1}	$\mu m^2\ s^{-1}$
Diffusion rate between $Al_{12}Mg_{17}$ and Mg	$D_{\gamma/Mg}$	$D_{Mg} \times 10^2$	$\mu m^2\ s^{-1}$
Diffusion rate between $Al_{12}Mg_{17}$ grains	$D_{GB,\gamma}$	$D_{Mg} \times 10^2$	$\mu m^2\ s^{-1}$
Mobility of the boundary $Al_{12}Mg_{17}$/Mg	$M_{\gamma/Mg}$	5.45×10^{-1}	$\mu m^2\ s^{-1}$
Mobility of grain boundaries	M_{GB}	5.45×10^{-1}	$\mu m^2\ s^{-1}$
Interface energy of the boundary $Al_{12}Mg_{17}$/Mg	$\Gamma_{\gamma/Mg}$	1.5×10^{-4}	$J\ \mu m^{-2}$
Interface energy of the grain boundaries	Γ_{GB}	$2\,\Gamma_{\gamma/Mg}$	$J\ \mu m^{-2}$
Lattice parameter of Mg (Han et al., 2015)	a_α	0.321	nm
Lattice parameter of Mg (Han et al., 2015)	c_α	0.521	nm
Lattice parameter of the $Al_{12}Mg_{17}$ (Han et al., 2015)	a_γ	1.056	nm
Lattice rotation (Han et al., 2015)	Θ	5.26	°

Finally, the Laplacian derived in Eqs. (23) (24) and presented in Eq. (25) can be evaluated for the two dimensional case as

$$\nabla^2\phi_{i,j} = \frac{1}{6\Delta x^2}[\phi_{i-1,j-1} + \phi_{i+1,j+1} + \phi_{i+1,j-1} + \phi_{i-1,j+1} + 4\phi_{i-1,j} + 4\phi_{i+1,j} + 4\phi_{i,j-1} + 4\phi_{i,j+1} - 20\phi_{i,j}]. \tag{45}$$

It is worth noting that, albeit a static momentum balance equation in Eq. (36) is solved, the time dependent displacement type boundary conditions are applied at a constant strain rate, accounting for the predicted strain and strain rate at different positions of the weld interface according to the results from the refill FSSW process simulation. Furthermore, the continuous phase transformation processes yield permanent changes by means of stress and strain within the domain, which are evaluated with the aforementioned numerical schemes.

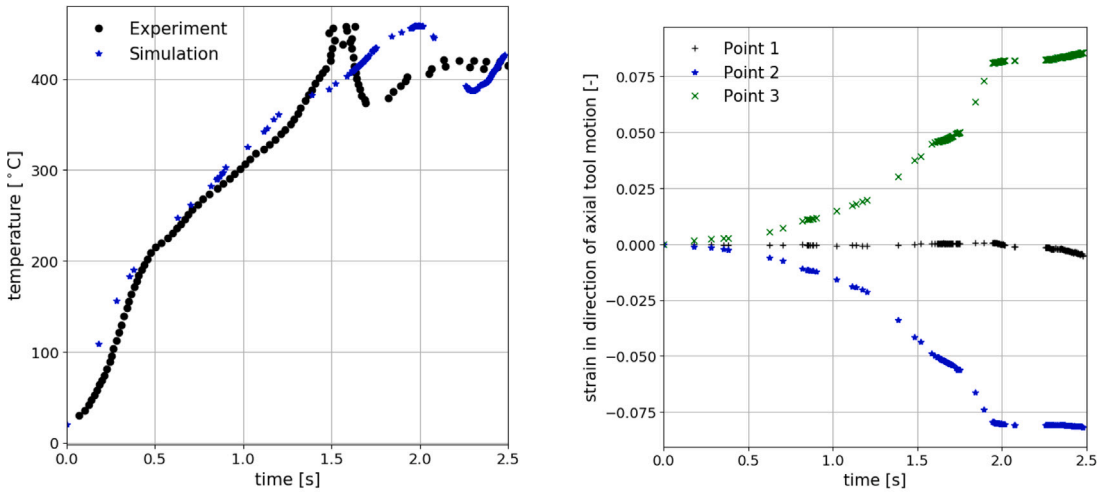

(a) (b)

Fig. 7. Results obtained from the process simulation of refill FSSW. (a) Temperature profile obtained from the simulation (star) and compared with the experiments (point). For this, Point 4 and 5 of Fig. 4(b), which are analogous to the position of the thermocouples used in Suhuddin et al. (2013), are evaluated. (b) Strain profiles obtained from the simulation. For strain, Point 1 (+), 2 (*), and 3 (x) in Fig. 4(a) are tracked. These results serve as the input parameters for the chemo-mechanical multiphase-field model.

4. Results

4.1. Process simulation of refill FSSW

The objective of the present study is to incorporate the mechanical effects on the evolution of intermetallic compounds. To this end, the refill FSSW process simulation intends to obtain the temperature and strain near the weld interface, where the focus is set to the end of the plunging phase. Fig. 7(a) shows the temperature evolution obtained from the simulations by tracking points 4 and 5, see Fig. 4(b), which are compared to the reported experimental measurements by Suhuddin et al. (2013).[5] Note that the simulation temperature illustrated in Fig. 7(a) is the average value obtained via evaluating Points 4 and 5. Similarly, the temperature from experiment is an average of the readings from two thermocouples. The simulation shows an acceptable agreement with the experimental measurement in terms of temperature. Since the evolution of the intermetallic compound is assumed isothermal in the subsequent sections due to the small domains considered in the multiphase field model, it is crucial to obtain the peak temperature that results in the maximum chemical driving force. The temperature peak obtained from the simulation and experiment is in good agreement, which is determined approximately as 450 °C. The free energy curves in Fig. 2 are computed using this peak temperature. Next to the temperature, the process simulation is, in particular, used to obtain the strain values in the direction of the tool motion near the weld center as shown in Fig. 4(b) for three points.

It can be seen that the material under the clamping ring barely experiences any strain while the material under the pin and sleeve moves in the opposite direction with a strain of ±8%, dividing the region of interest for intermetallic phase formations into two categories:

1. presence of eigenstrain and no external strain
2. presence of eigenstrain and maximum |8|% external strain

The isothermal characteristic of the problem renders phase transformation as inevitable and thus prescribes the existence of eigenstrain even when there is no external strain.

In the following, the evolution of intermetallic compounds in the presence of various driving forces is investigated using the output of the performed refill FSSW process simulation. Note that the temperature and strain are computed at the weld interface via the FE based refill FSSW process simulation using a macro scale domain (mm), whereas the investigations of the intermetallic compound evolution via multiphase field simulations are carried out using a micro scale domain (μm). In such a smaller domain, the temperature and strain are assumed constant.[6] As a consequence, the problem is assumed to be isothermal. Section 4.2 shows

[5] Points 4 and 5 correspond to the location of the thermocouples embedded in the joint area by Suhuddin et al. (2013). Since the sleeve does not plunge into the weld center, potential thermal disruptions were avoided.

[6] Based on the previous studies on large-scale multiphase-field simulations, e.g., Steinmetz et al. (2016) and Hötzer et al. (2015), investigations of intermetallic compound evolution at the weld interface can be extended to bigger scales – expected to be computationally expensive – in the future, which accounts for temperature and strain gradients..

the evolution in the absence of strain, i.e., purely a chemical case. The temperature T is introduced in the multiphase field model through Eq. (8), where chemical free energy density f_α^{chem} is computed via CALPHAD at the peak temperature of 450 °C obtained from the process simulation.[7] To account for strain variation, Sections 4.4 and 4.5 depict the intermetallic compounds' evolution in the presence of solely eigen strain and a combination of eigen and external strain, respectively, representing various regions of interest of the weld interface mentioned earlier. The total strain ε is introduced in the multiphase field model via Eqs. (10) and (11) through ε_α, where $\varepsilon = 8\% = \sum_\alpha \varepsilon_\alpha h_\alpha$ was obtained from the process simulation. Finally, the eigen strain ε_α^0 (calculated in Eqs. (37) and (38)) that represents the stress free transformation strain induced as a result of crystal structure differences between the two evolving phases, is introduced in the multiphase field model via non elastic strain $\tilde{\varepsilon}_\alpha$ in Eq. (12).

4.2. Morphology and thickness evolution of the intermetallic compound driven by purely chemical forces

Initially, the purely chemical multiphase field model of Eqs. (23) and (31) is used to simulate the evolution of $Al_{12}Mg_{17}$ in the Mg matrix driven by only temperature. With the material parameters set in Table 4, Fig. 8 exhibits the evolution of the intermetallic compound $Al_{12}Mg_{17}$ at various time steps during the simulation. In the early stages, a deviation of the concentrations with respect to the corresponding equilibrium concentrations of the phases is present, which induces a driving force for phase transformation. These differences converge to zero approaching the final stages of the simulation,[8] i.e., chemical equilibrium is reached, and the driving force is vanishing. A closer look at the evolution of the intermetallic compound in the early stages of transformation in Fig. 8 reveals some coalescing effects besides regular grain growth characteristics. Since the intermetallic grains are initially randomly distributed and slightly differ in terms of size, coalescence behavior is expected and in agreement with experimental and theoretical investigations of Mullins (1956), Nichols and Mullins (1965) and Nichols (1966), which show grain boundary motion and coalescence effects accounting for shape and size effects. During the simulation, the evolution continues to be governed by the same mechanisms as the bigger grains keep on growing faster at the expense of the neighboring smaller grains. Due to the locally different growth rates between the intermetallic grains, the overall thickness of the intermetallic layer tends to vary across the welding zone's cross section, also observed by Suhuddin et al. (2014) experimentally. For the sake of comparing the resulting microstructures with our previous work (Raza and Klusemann, 2020), the averaged mean thickness of the intermetallic compound at chemical equilibrium obtained from the purely chemically driven evolution is ~3.6 μm which yields a reasonable agreement considering the temperature and initial configuration are slightly different between the two investigations. Experimentally, Suhuddin et al. (2014) measured the combined thickness of intermetallic compounds, i.e., Al_3Mg_2 and $Al_{12}Mg_{17}$, to be in the range of 7 20 μm, 7 μm was observed at locations where tool movement did not influence the material flow, while the 20 μm were determined at areas affected by the tool movement. Thus the lower end of the measured thickness range corresponds to the purely chemical case (Raza and Klusemann, 2020). Assuming that both intermetallic compounds grow similarly, the $Al_{12}Mg_{17}$ intermetallic compound thickness observed by Suhuddin et al. (2014) is 3.5 μm, comparing well with the simulation thickness of ~3.6 μm.

Next, the impact of interface energy and initial grain distribution on the grain growth front is investigated.

4.3. Morphological dependency of the intermetallic layer on the interface energy and initial grain distribution

The final microstructure of the intermetallic compound depends on the selected interface energy and initial configuration of the pre existing grains. As aforementioned, the interface energies are difficult to measure experimentally or to obtain computationally, hence an appropriate breakdown of the effective interface energy landscape is hard to accomplish as well. Therefore, to take into account two different possible constellations of the interface energies, Fig. 8 is prescribed with $\Gamma_{\gamma/\text{Mg}} = 1.5 \times 10^{-4}\,\text{J}\,\mu\text{m}^{-2}$ and $\Gamma_{\text{GB}} = 2\,\Gamma_{\gamma/\text{Mg}}\,\text{J}\,\mu\text{m}^{-2}$, while Fig. 9 is calculated with $\Gamma_{\gamma/\text{Mg}} = 2.5 \times 10^{-4}\,\text{J}\,\mu\text{m}^{-2}$ and $\Gamma_{\text{GB}} = 2\,\Gamma_{\gamma/\text{Mg}}\,\text{J}\,\mu\text{m}^{-2}$. Furthermore, the initial grain sizes are varied as displayed in Fig. 9(g) and denoted by I, II, and III. The grain distribution of the computation labeled II (Figs. 9(c) and 9(d)) is identical with the initial configuration in Fig. 8, so that the final states can directly be compared. The final morphologies in Figs. 8(f) and 9(d) emerge differently: it can be observed that the higher interfacial energies favor coalescing behavior (Raza and Klusemann, 2020). Similar observations were made by Park and Arróyave (2012) and Huh et al. (2004) in investigations involving intermetallic compounds evolution (albeit in a different material system involving Cu and Sn), where higher interfacial energies resulted in enhanced coalescence and thus higher coarsening of the intermetallic grains. Other investigations, such as Ma et al. (2006), based on multiphase field methods, yield insights into how interfacial energies can affect the shape and coalescence grain behavior. Additionally, similar findings were identified in other material systems, e.g. carbon materials (Smith et al., 1985) and polymer colloids (Dobler et al., 1992). Although the morphology emerges differently in the two cases, it is worth noting that the average layer thickness remains the same, i.e., irrespective of the change in interface energy.

Next, to understand the influence of the positioning of the initially larger grains on the homogeneity of the growth front, three cases denoted by the superscripts I, II, and III in Fig. 9 are set up. The black framed grains in the magnifications, Fig. 9(g), illustrate the position of the larger grains compared to the others in the respective distribution. It can be seen that the locations and grain sizes are varied to account for the influence of size effect on the final intermetallic morphology. These changes in the final microstructure Figs. 9(b), 9(d), 9(f), although the grains have identical properties, are due to the slight initial difference in grain size, corresponding to Figs. 9(a), 9(c), 9(e), respectively. Having a size/volumetric advantage from the start of the evolution helps those larger grains to compete against smaller grains. This competition between the intermetallic compound grains eventually leads to grains coalescing in a first step, followed by grain coarsening phenomena, as observed in the resulting microstructures.

[7] As the problem is considered isothermal, the evolution of intermetallic compound is computed at the peak temperature $T = 450$ °C which induces the maximum chemical driving force.

[8] Here the final stage of the multiphase-field simulation represents the end of the plunging stage of the refill FSSW process.

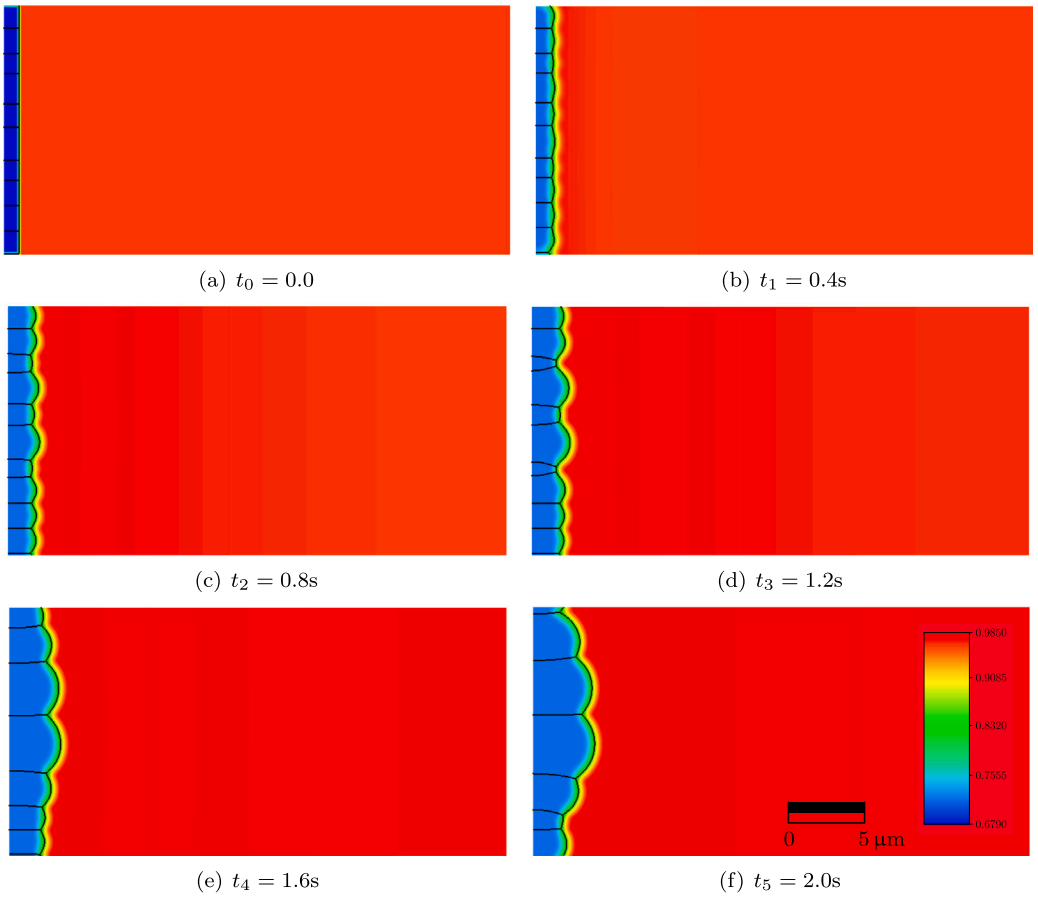

Fig. 8. Evolution of intermetallic compound driven only by chemical forces at different stages of the simulation based on the material properties set in Table 4. The black isolines represent phase and grain boundaries between the intermetallic grains, while the underlying colormap depicts the amount of Mg in mole fraction. The initial composition of $Al_{12}Mg_{17}$ and Mg is assumed to be 0.679 and 0.985, respectively.

Fig. 10 is set with the initial configuration corresponding to Figs. 9(a) and 9(b) and interface energies as $\Gamma_{\gamma/\mathrm{Mg}} = 2.5 \times 10^{-4}$J µm^{-2} and $\Gamma_{\mathrm{GB}} = 2\,\Gamma_{\gamma/\mathrm{Mg}}$ J µm^{-2}, leading to a homogeneous growth front and an appropriate growth and coalescence behavior of intermetallic compound grains, in accordance with the experimental study (Suhuddin et al., 2014). Fig. 10 shows the evolution of the intermetallic compounds at various stages of the simulation. Any thermodynamically governed phase transformation process is an endeavor to even out differences in chemical potentials in order to reach an equilibrium state (Ankit et al., 2014). This equilibrium state is accomplished by migration of the corresponding chemical species (Chen, 2019), i.e., diffusion. Thus, the corresponding chemical species travels along diffusion paths from regions with high chemical potential to regions with low chemical potential. According to Ankit et al. (2015) and Mittnacht et al. (2019), the more complex the grain distribution appears to be, the more complex the evolving diffusion paths tend to look like.

4.4. Morphology and thickness evolution of intermetallic compounds driven by chemical and mechanical (eigenstrain) forces

Using Eq. (38), therein reducing the dimensions according to the two dimensional framework and inserting the corresponding lattice parameters, Table 4, the eigenstrain is calculated to be ±5%, while the shear components are computed as −1%. Since the present model solely captures elastic effects, the calculated eigenstrain involves a prefactor to account for any plastic accommodations (Schoof et al., 2020). The prefactor is chosen to be 0.5 to keep possible plastifications due to lattice differences as low as possible without artificially scaling the elastic influence too far down. Using these values of eigenstrain in the matrix phase and the grain and concentration setup as in Fig. 8, Fig. 11 shows the evolution of $Al_{12}Mg_{17}$ intermetallic compound in Mg. One can observe that the peak stress value reaches around 100 MPa. A higher prefactor would cause higher stresses above the yield strength of Mg, respectively AZ31, which conversely would mean plastifications in the material that is beyond the scope of the current framework. The boundary conditions for phase field and concentration are kept same as in the chemical model. In terms of mechanical boundary conditions, the previously assumed periodicity along the y axis is still pursued. However, along x direction the left edge of the domain is fixed with a Dirichlet condition and the right edge is preset as stress free.

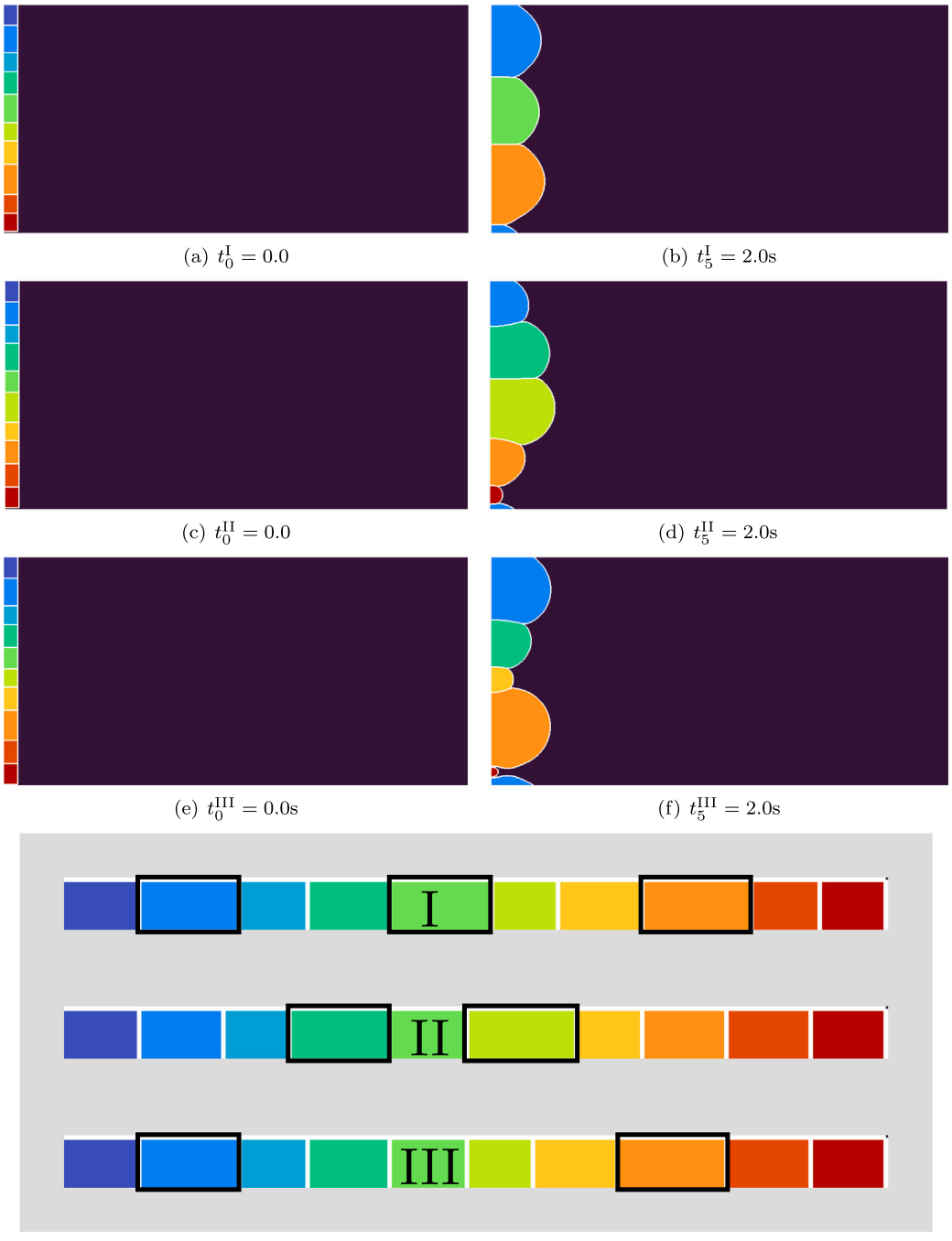

Fig. 9. Evolution of intermetallic compound driven only by chemical forces at the first and the last time step of the simulation based on the material properties set in Table Table 4. To illustrate the pronounced impact of initial configuration on the overall intermetallic compound morphology, the interface energies are kept as: $\Gamma_{\gamma/\mathrm{Mg}} = 2.5\times10^{-4}\,\mathrm{J\ \mu m^{-2}}$ and $\Gamma_{\mathrm{GB}} = 2\,\Gamma_{\gamma/\mathrm{Mg}}\ \mathrm{J\ \mu m^{-2}}$. The white lines represent the isolines of the $Al_{12}Mg_{17}$ grains. To better distinguish individual grains from each other, those are pigmented individually for (a) to (f). In (g), the initial grain distributions are magnified to illustrate geometrical differences within the layer. The black-framed grains in each distribution are the placed significantly larger grains. Figure Fig. 8 corresponds to the configuration in (c) and (d) while Figure Fig. 10 to the configuration in (a) and (b).

The additional driving force in the form of eigenstrain has an evident effect on the growth of the intermetallic layer as it yields further tensile forces. Considering the early stages of transformation with chemo mechanically coupled driving forces makes it worth noting that the additional mechanical contribution seems to have a dominant effect on the driving forces. One cause of this

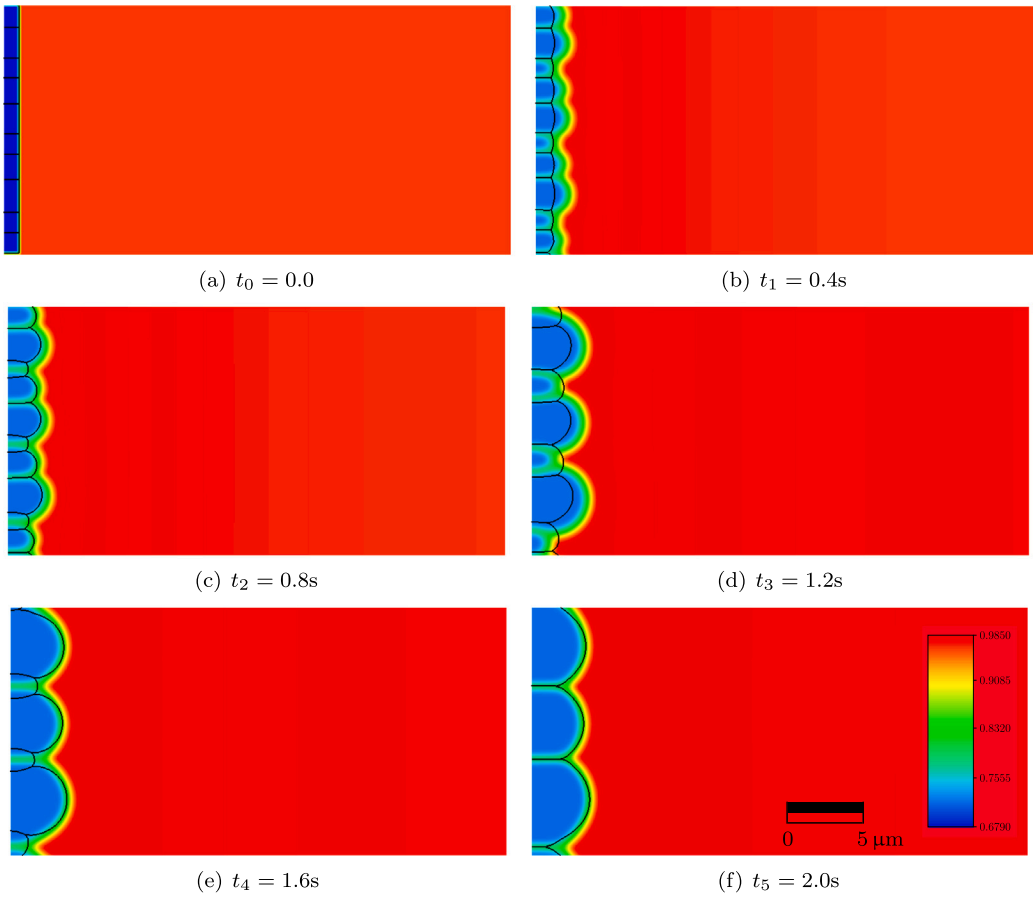

Fig. 10. Evolution of intermetallic compound driven only by chemical forces at different stages of the simulation based on the material properties set in Table 4 apart from the interface energies that are altered as: $\Gamma_{\gamma/\mathrm{Mg}} = 2.5 \times 10^{-4}$J µm^{-2} and $\Gamma_{\mathrm{GB}} = 2\,\Gamma_{\gamma/\mathrm{Mg}}$ J µm^{-2}. The black lines illustrate the isolines of the $Al_{12}Mg_{17}$ grains. The underlying colormap depicts the amount of Mg in mole fraction. The initial composition of $Al_{12}Mg_{17}$ and Mg is assumed to be 0.679 and 0.985, respectively.

morphology evolution is the magnitude of eigenstrain, which can be classified as considerable in the present framework tailored for small deformations. The dominance of the mechanical driving force induced by the eigenstrain is reflected in multiple manners: The resulting microstructure is affected by the mechanical contribution in terms of layer thickness. Due to the presence of eigenstrain, the average layer thickness increases to 5.2 µm (in Fig. 11) compared to 3.6 µm (in Fig. 8), leading further to close the gap between experimentally and numerically obtained thicknesses. Furthermore, the coalescing behavior of the grains alters as well. The shown stress distribution indicates that peak values are formed immediately ahead of the growth front throughout the evolution, whereas in the bulk region of the grains, the stresses are considerably less pronounced. The emerging stress gradient accelerates the intermetallic layer growth.

4.5. Morphology and thickness evolution of intermetallic compounds driven by chemical and mechanical (eigen and external strain) forces

Using the computed eigenstrain in the previous section and applying the additional external strain of +8% determined via the refill FSSW process simulation, Fig. 12 shows the evolution of $Al_{12}Mg_{17}$. The external strain is brought into the system via time dependent displacement boundary conditions (Amos et al., 2018; Schneider et al., 2017), applied in normal direction at the left and right edges of the domain. Applying the 8% strain at once is not physical and might lead to numerical instabilities additionally, since the sleeve needs some time to plunge into the material. In this regard, the displacement is applied at a constant strain rate, approximately to the average strain rate in the refill FSSW process simulation, see Fig. 7(b).

The driving force for intermetallic compound growth is divided into two categories: chemical and mechanical, whereas the mechanical driving force is further subdivided into eigenstrain and strain occurring due to external loading. Fig. 12 reveals early on that the external strain influences the morphological evolution considerably. The intermetallic compound grains that are favored in the early stages of the transformation tend to consume the surrounding inferior grains even faster than in the case where only eigenstrain is present (as per Fig. 11), i.e., further pronounced coarsening takes place. Additionally, a significant increase

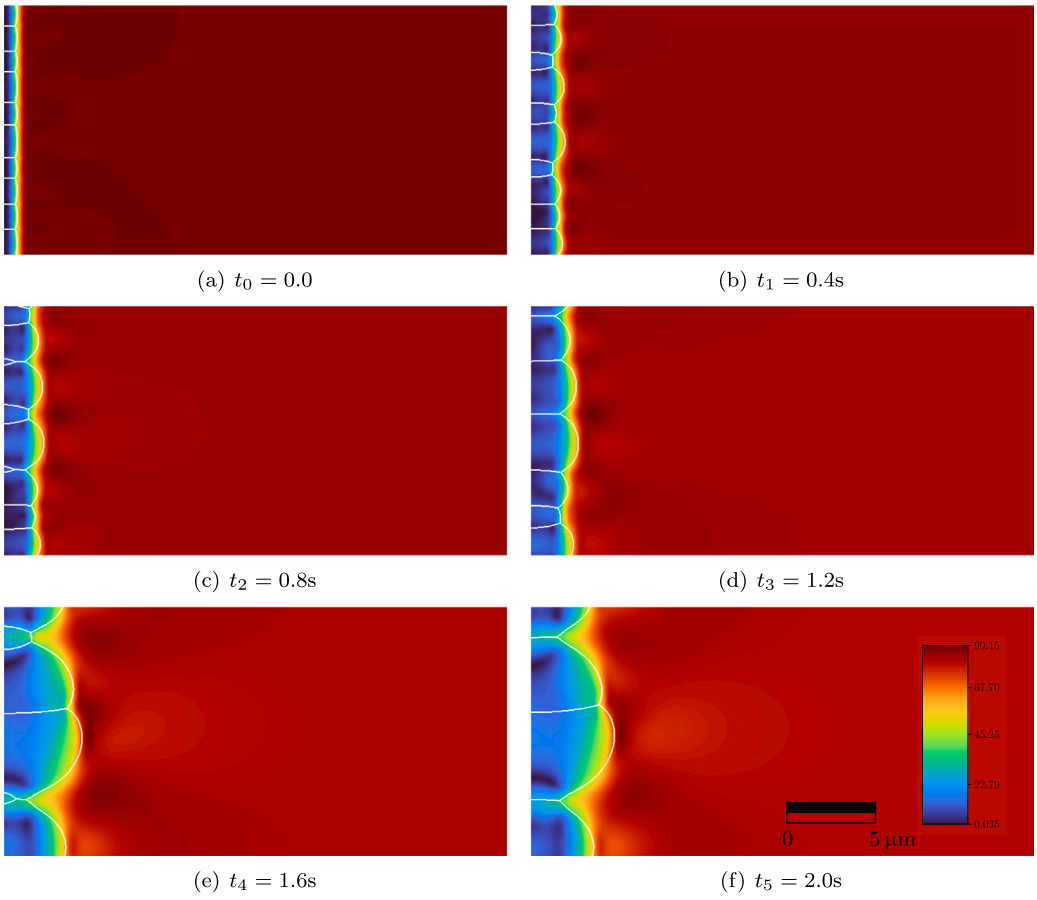

Fig. 11. Evolution of intermetallic compound driven by chemical forces and eigenstrain at different stages of the simulation based on the material properties set in Table 4. White lines are isolines for phase boundaries, and the colormap displays von-Mises stress distribution, where the unit is given in MPa. The initial microstructure corresponds to the II-configuration in Fig. 9.

of the intermetallic layer thickness can be observed. The average thickness yielded by the simulation is found to be 6.2 µm. The incorporation of mechanical driving force leads to a shift in Gibbs energy curves of the phases, i.e., change in Gibbs energies and/or change in equilibrium concentration.

Fig. 13(a) depicts the evolution kinetics of the intermetallic layer in the presence of various driving forces during the plunging stage of refill FSSW process: The purely chemical model exhibits the slowest intermetallic layer kinetics (black); however, the intermetallic compound evolution reaches equilibrium at the end of the 2 s time period. The chemo mechanically driven model that considers external strain in addition to the eigenstrain (green) shows accelerated growth compared to the case when only eigenstrain is considered (blue). It is crucial to point out that at the end of the plunging stage, the intermetallic compound growth based on the chemo mechanical model does not achieve equilibrium and is likely to grow beyond the plunging stage. This behavior can be observed in Fig. 13 since in the purely chemical case the intermetallic growth velocity converges to 0 after 2 s, whereas the chemo mechanically cases are yet to reach vanishing growth velocity, i.e., the intermetallic will likely continue growing after 2 s, exhibiting growth with non equilibrium concentration. Fig. 13(b) shows the growth of intermetallic compound driven by temperature and strain beyond the plunging stage (i.e., after 2 s). It is seen that the intermetallic growth achieves equilibrium after the dwelling stage (i.e., after 4 s). Based on these findings, it is worth noting that the addition of mechanical forces induces a shift of the holistic equilibrium state of the system.

Furthermore, in Fig. 13, the observations made by Suhuddin et al. (2014) are also incorporated. In an Al Mg system that shows the appearance of Al_3Mg_2 and $Al_{12}Mg_{17}$ intermetallic compound during refill FSSW, the overall intermetallic layer, i.e., of Al_3Mg_2 and $Al_{12}Mg_{17}$ together, is found in the range of 7 20 µm after the process, showing an overall process time of 6 s. As mentioned in Section 4.2, the lower end of the thickness range represents the purely chemical case; similarly, the maximum of the thickness range corresponds to the chemo mechanical case. The $Al_{12}Mg_{17}$ intermetallic compound thickness is found to be 3.5 µm (red diamond in Fig. 13(a)) and 10 µm (red square in Fig. 13(b)), respectively, assuming that both intermetallic compounds (Al_3Mg_2 and $Al_{12}Mg_{17}$) grow equally. The $Al_{12}Mg_{17}$ intermetallic compound thickness obtained from the current chemically driven model agrees well with the lower thickness obtained experimentally, especially considering that the chemically driven model reaches equilibrium after 2 s.

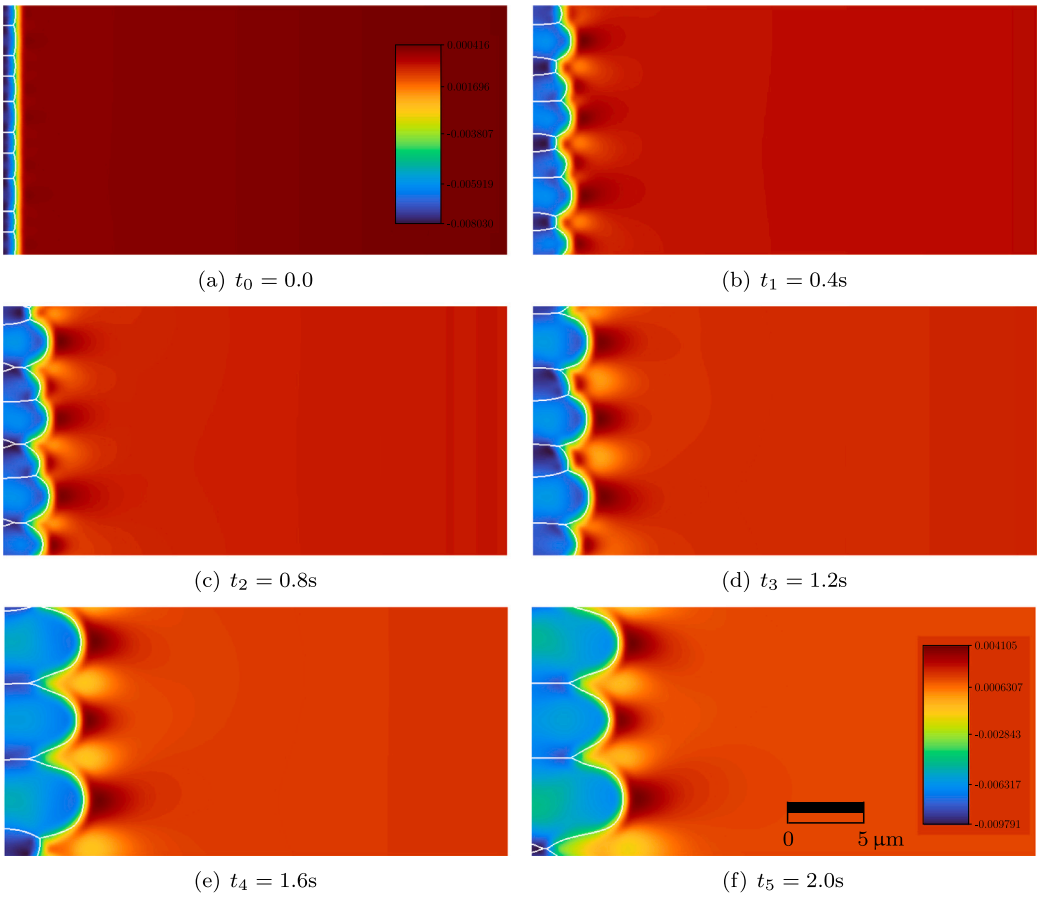

Fig. 12. Evolution of the intermetallic compound driven by chemical and mechanical forces at different stages of the simulation based on the material properties set in Table 4. The mechanical driving forces are (i) eigenstrain accounting for strain resulting from crystal structure differences and (ii) strain resulting from externally applied displacement catering for the plunging process. The white lines are isolines for phase boundaries, and the colormap displays strain distribution (ϵ_{xx}). Note that in (a) the values represent the strain in x-axis due to eigenstrain, as the external strain is increasing onwards from t_0.

This lower thickness was found in the weld zone, where nearly no strain was present. In contrast, the chemo mechanically driven model represents an acceptable agreement to the larger thickness obtained experimentally at the positions where tool movement strongly influences the material flow. Overall, the multiphase field simulation provides a reasonable agreement of intermetallic compound thicknesses along the weld, driven by different contributions.

5. Conclusion

As the thickness of the intermetallic compounds affects the lap shear strength of joints (Suhuddin et al., 2014) produced by friction based joining processes, it is vital to predict this thickness at the joint interface. In the solid state joining of dissimilar materials, the weld interface is subjected to temperature and strain, leading to two driving mechanisms for intermetallic compounds: chemical and mechanical. The current study incorporates chemical as well as mechanical driving forces to the multiphase field model to investigate the effect of both contributions on the layer thickness, morphology, and growth dynamics. During the refill FSSW of Al and Mg, the intermetallic compound $Al_{12}Mg_{17}$ and on the Mg side of the couple is investigated in the presence of chemical and mechanical driving forces.

To obtain quantitative temperature and strain profiles at the weld interface, a process simulation of refill FSSW based on the FE method is set up in DEFORM3D and compared with experimental results from Suhuddin et al. (2013). The temperature profile obtained from the simulation shows reasonable agreement to the experimental measurements. The strain profile indicates that the material flow due to the tool motion during the plunging stage categorizes the weld interface into two regions: one experiences strain that is induced due to the motion of the tool, i.e., external strain and the other does not. However, the isothermal nature of the problem indicates that in both cases, presence of strain due to the difference in crystal structure between $Al_{12}Mg_{17}$ intermetallic compound and Mg bulk phase, i.e., eigenstrain, is present. The temperature and strain information serve as input parameters for the multiphase field model.

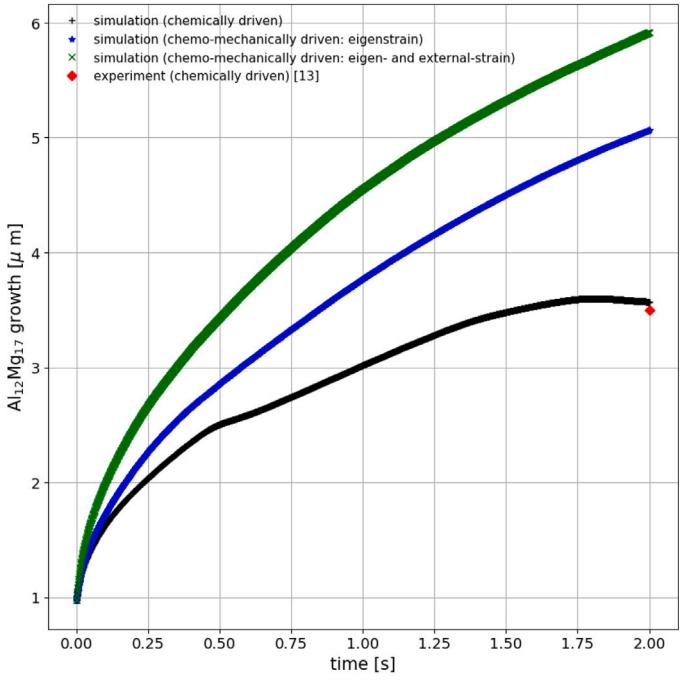

(a)

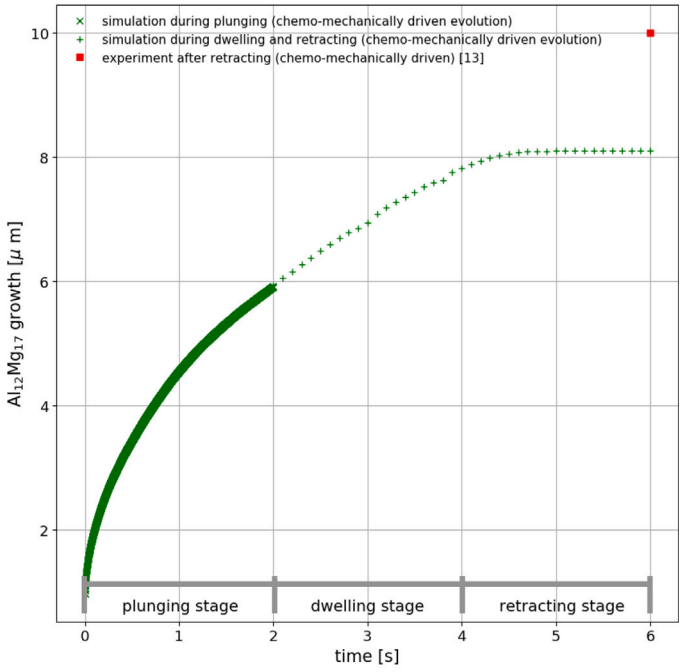

(b)

Fig. 13. Evolution kinetics of the $Al_{12}Mg_{17}$ intermetallic compound driven chemically, mechanically with eigenstrain, and with eigen- as well as external- strain, showing faster growth with the addition of mechanical driving forces. The $Al_{12}Mg_{17}$ intermetallic compound thickness obtained from Suhuddin et al. (2014) with the assumption of equal split between Al_3Mg_2 and $Al_{12}Mg_{17}$ intermetallic compounds is also incorporated in the plot for comparison. Note that only the lower end of the range obtained by Suhuddin et al. (2014), i.e., 3.5 μm is plotted for comparison with the purely chemical driven case in (a), while the higher end of the range, i.e., 10 μm is plotted for comparison with the chemo-mechanical case in (b).

The developed chemo mechanical multi phase field model accounts next to chemical driving forces for the contribution of eigenstrain due to phase transformation and external strain induced by the tool. CALPHAD method is utilized for the computation of the chemical free energy density. The model is capable of showing the $Al_{12}Mg_{17}$ intermetallic compound growth in the Mg phase and predicting the morphology as well as the thickness in the presence of various driving forces. Initially, a purely chemical driven evolution of the $Al_{12}Mg_{17}$ in the Mg phase is investigated. The influence of interface energy and initial microstructure is observed to play a vital role in the final morphology of the intermetallic compounds. Next, the eigenstrain is introduced in the model, and the simulation leads to a thicker intermetallic layer as well as enhanced kinetics and coarsening. Finally, the external strain is added in a linearly ramped up manner (constant strain rate) as mechanical boundary conditions, and it is observed that the final thickness of the intermetallic compound layer becomes larger and thus leads to a reasonable agreement with the higher end of the measured thickness by Suhuddin et al. (2014).

Combining numerical approaches such as finite element and multiphase field methods can provide a framework for predicting the intermetallic compound thickness at the interface of joints of dissimilar material produced by friction based joining processes. Future investigations may involve large scale multiphase field simulation based on previous works (Hötzer et al., 2015; Steinmetz et al., 2016) to investigate the stoichiometric Al_3Mg_2 and non stoichiometric $Al_{12}Mg_{17}$ at the weld interface of the Al and Mg joint. The framework presented in this study can be used to investigate the intermetallic compound evolution in various solid state joining processes and material systems. The prediction of intermetallic compound layer thickness, morphology, and kinetics information presents a future opportunity to get insight into the joint strength produced by solid state joining processes.

CRediT authorship contribution statement

Syed Hasan Raza: Conceptualization, Methodology, Validation, Investigation, Writing original draft, Writing review & editing, Data curation, Visualization, Project administration. **Tobias Mittnacht:** Conceptualization, Methodology, Validation, Investigation, Writing original draft, Writing review & editing, Data curation, Visualization. **George Diyoke:** Methodology, Validation, Investigation, Writing review & editing, Visualization. **Daniel Schneider:** Conceptualization, Software, Supervision, Writing review & editing, Funding acquisition. **Britta Nestler:** Conceptualization, Supervision, Writing review & editing, Funding acquisition. **Benjamin Klusemann:** Conceptualization, Supervision, Writing review & editing, Funding acquisition.

Declaration of competing interest

The authors declare that they have no known competing financial interests or personal relationships that could have appeared to influence the work reported in this paper.

Data availability

Data will be made available on request.

Acknowledgments

The authors gratefully acknowledge financial support of the research through the programmes “Virtual Materials Design” and “Material Systems Engineering (MSE)” of the Helmholtz association. Data and data processing are provided within the KNMFi and MDMC initiatives (no. 43.31.01) through the research data infrastructure Kadi4Mat [https://kadi.iam cms.kit.edu].

Benjamin Klusemann gratefully acknowledges partial funding by the Deutsche Forschungsgemeinschaft (DFG, German Research Foundation) project number 464986536.

References

Abbassi, F., Srinivasan, M., Loganathan, C., Narayanasamy, R., Gupta, M., 2016. Experimental and numerical analyses of magnesium alloy hot workability. J. Magn. Alloys 4 (4), 295–301.

AFGHAHI, S.S.S., Jafarian, M., Paidar, M., Jafarian, M., 2016. Diffusion bonding of Al 7075 and Mg AZ31 alloys: Process parameters, microstructural analysis and mechanical properties. Trans. Nonferr. Met. Soc. China 26 (7), 1843–1851.

Amos, P.K., Schoof, E., Schneider, D., Nestler, B., 2018. Chemo-elastic phase-field simulation of the cooperative growth of mutually-accommodating widmanstätten plates. J. Alloys Compd. 767, 1141–1154.

Ankit, K., Mittnacht, T., Mukherjee, R., Nestler, B., 2015. Evolution of mixed cementite morphologies during non-cooperative eutectoid transformation in Fe–C steels. Comput. Mater. Sci. 108, 342–347.

Ankit, K., Mukherjee, R., Mittnacht, T., Nestler, B., 2014. Deviations from cooperative growth mode during eutectoid transformation: Insights from a phase-field approach. Acta Mater. 81, 204–210.

Apel, M., Böttger, B., Rudnizki, J., Schaffnit, P., Steinbach, I., 2009. Grain growth simulations including particle pinning using the multiphase-field concept. ISIJ Int. 49 (7), 1024–1029.

Awang, M., Mucino, V.H., 2010. Energy generation during friction stir spot welding (FSSW) of Al 6061-T6 plates. Mater. Manuf. Process. 25 (1–3), 167–174.

Bellemans, I., Moelans, N., Verbeken, K., 2018. Phase-field modelling in extractive metallurgy. Crit. Rev. Solid State Mater. Sci. 43 (5), 417–454.

Böttger, B., Schmitz, G., Santillana, B., 2012. Multi-phase-field modeling of solidification in technical steel grades. Trans. Indian Inst. Met. 65 (6), 613–615.

Brennan, S., Bermudez, K., Kulkarni, N.S., Sohn, Y., 2012. Interdiffusion in the Mg-Al system and intrinsic diffusion in β-Mg2Al3. Metall. Mater. Trans. A 43 (11), 4043–4052.

Cahn, J., Allen, S., 1977. A microscopic theory for domain wall motion and its experimental verification in Fe-Al alloy domain growth kinetics. J. Phys. Colloq. 38 (C7), C7–51.

Campanelli, L.C., Suhuddin, U.F.H., Antonialli, A.Í.S., Dos Santos, J.F., De Alcantara, N.G., Bolfarini, C., 2013. Metallurgy and mechanical performance of AZ31 magnesium alloy friction spot welds. J. Mater Process. Technol. 213 (4), 515–521.
Chen, L.-Q., 2002. Phase-field models for microstructure evolution. Annu. Rev. Mater. Res. 32 (1), 113–140.
Chen, L.-Q., 2019. Chemical potential and Gibbs free energy. MRS Bull. 44 (7), 520–523.
Chen, C.-Y., Chen, H.-L., Hwang, W.-S., 2006. Influence of interfacial structure development on the fracture mechanism and bond strength of aluminum/copper bimetal plate. Mater. Trans. 47 (4), 1232–1239.
Chen, W., Wang, W., Liu, Z., Zhai, X., Bian, G., Zhang, T., Dong, P., 2021. Improvement in tensile strength of Mg/Al alloy dissimilar friction stir welding joints by reducing intermetallic compounds. J. Alloys Compd. 861, 157942.
Chen, G., Zhang, S., Zhu, Y., Yang, C., Shi, Q., 2020. Thermo-mechanical analysis of friction stir welding: A review on recent advances. Acta Metall. Sin. (Engl. Lett.) 33 (1), 3–12.
Choudhury, A., Nestler, B., 2012. Grand-potential formulation for multicomponent phase transformations combined with thin-interface asymptotics of the double-obstacle potential. Phys. Rev. E 85 (2), 021602.
Dobler, F., Pith, T., Lambla, M., Holl, Y., 1992. Coalescence mechanisms of polymer colloids: I. Coalescence under the influence of particle-water interfacial tension. J. Colloid Interface Sci. 152 (1), 1–11.
Effertz, P., Infante, V., Quintino, L., Suhuddin, U., Hanke, S., Dos Santos, J., 2016. Fatigue life assessment of friction spot welded 7050-T76 aluminium alloy using Weibull distribution. Int. J. Fatigue 87, 381–390.
Eiken, J., Böttger, B., Steinbach, I., 2006. Multiphase-field approach for multicomponent alloys with extrapolation scheme for numerical application. Phys. Rev. E 73.
Gerlich, A., Su, P., North, T., 2005. Peak temperatures and microstructures in aluminium and magnesium alloy friction stir spot welds. Sci. Technol. Weld. Join. 10 (6), 647–652.
Han, G., Han, Z., Luo, A.A., Liu, B., 2015. Three-dimensional phase-field simulation and experimental validation of β-$Mg_{17}Al_{12}$ phase precipitation in Mg-Al-based alloys. Metall. Mater. Trans. A 46 (2), 948–962.
Handbook, A., 1992. Vol. 1, 2 Metals Handbook, Vol. 3 Alloy Phase Diagram. ASM International, Materials Park Ohio, USA.
He, X., Gu, F., Ball, A., 2014. A review of numerical analysis of friction stir welding. Prog. Mater. Sci. 65, 1–66.
Hong, K., Huh, J.Y., 2006. Phase field simulations of morphological evolution and growth kinetics of solder reaction products. J. Electron. Mater. 35 (1), 56–64.
Hötzer, J., Jainta, M., Steinmetz, P., Nestler, B., Dennstedt, A., Genau, A., Bauer, M., Köstler, H., Rüde, U., 2015. Large scale phase-field simulations of directional ternary eutectic solidification. Acta Mater. 93, 194–204.
Hötzer, J., Reiter, A., Hierl, H., Steinmetz, P., Selzer, M., Nestler, B., 2018. The parallel multi-physics phase-field framework Pace3D. J. Comput. Sci. 26, 1–12.
Hötzer, J., Seiz, M., Kellner, M., Rheinheimer, W., Nestler, B., 2019. Phase-field simulation of solid state sintering. Acta Mater. 164, 184–195.
Huh, J., Hong, K., Kim, Y., Kim, K., 2004. Phase field simulations of intermetallic compound growth during soldering reactions. J. Electron. Mater. 33 (10), 1161–1170.
Jafarian, M., Rizi, M.S., Jafarian, M., Honarmand, M., Javadinejad, H.R., Ghaheri, A., Bahramipour, M.T., Ebrahimian, M., 2016. Effect of thermal tempering on microstructure and mechanical properties of Mg-AZ31/Al-6061 diffusion bonding. Mater. Sci. Eng. A 666, 372–379.
Jain, R., Pal, S.K., Singh, S.B., 2018. Thermomechanical simulation of friction stir welding process using Lagrangian method. In: Simulations for Design and Manufacturing. Springer Singapore, pp. 103–146.
Janga, V.S.R., Awang, M., Yamin, M.F., Suhuddin, U.F.H., Klusemann, B., Santos, J.F.d., 2021. Experimental and numerical analysis of refill friction stir spot welding of thin AA7075-T6 sheets. Materials 14 (23).
Ji, S., Li, Z., Wang, Y., Ma, L., Zhang, L., 2017a. Material flow behavior of refill friction stir spot welded LY12 aluminum alloy. High Temp. Mater. Process. 36 (5), 495–504.
Ji, S., Wang, Y., Li, Z., Yue, Y., Chai, P., 2017b. Effect of tool geometry on material flow behavior of refill friction stir spot welding. Trans. Indian Inst. Met. 70 (6), 1417–1430.
Kim, H.-S., Lee, H.-J., Yu, Y.-S., Won, Y.-S., 2009. Three-dimensional simulation of intermetallic compound layer growth in a binary alloy system. Acta Mater. 57 (4), 1254–1262.
Kulkarni, K.N., Luo, A.A., 2013. Interdiffusion and phase growth kinetics in magnesium-aluminum binary system. J. Phase Equilib. Diffus. 34 (2), 104–115.
Lee, C.-Y., Choi, D.-H., Yeon, Y.-M., Jung, S.-B., 2009. Dissimilar friction stir spot welding of low carbon steel and Al–Mg alloy by formation of IMCs. Sci. Technol. Weld. Join. 14 (3), 216–220.
Liu, L., Ren, D., Liu, F., 2014. A review of dissimilar welding techniques for magnesium alloys to aluminum alloys. Materials 7 (5), 3735–3757.
Liyanage, T., Kilbourne, J., Gerlich, A., North, T., 2009. Joint formation in dissimilar Al alloy/steel and Mg alloy/steel friction stir spot welds. Sci. Technol. Weld. Join. 14 (6), 500–508.
Luo, A., Zhang, C., Sachdev, A., 2012. Effect of eutectic temperature on the extrudability of magnesium–aluminum alloys. Scr. Mater. 66 (7), 491–494.
Ma, N., Chen, Q., Wang, Y., 2006. Implementation of high interfacial energy anisotropy in phase field simulations. Scr. Mater. 54 (11), 1919–1924.
McLean, A., Powell, G., Brown, I., Linton, V., 2003. Friction stir welding of magnesium alloy AZ31B to aluminium alloy 5083. Sci. Technol. Weld. Join. 8 (6), 462–464.
Meyghani, B., Awang, M.B., Emamian, S.S., Mohd Nor, M.K.B., Pedapati, S.R., 2017. A comparison of different finite element methods in the thermal analysis of friction stir welding (FSW). Metals 7 (10), 450.
Militzer, M., Azizi-Alizamini, H., 2011. Phase field modelling of austenite formation in low carbon steels. In: Solid State Phenomena, Vol. 172. Trans Tech Publ, pp. 1050–1059.
Minamoto, S., Nomoto, S., Hamaya, A., Horiuchi, T., Miura, S., 2010. Microstructure simulation for solidification of magnesium–zinc–yttrium alloy by multi-phase-field method coupled with CALPHAD database. ISIJ Int. 50 (12), 1914–1919.
Mittnacht, T., Amos, P., Schneider, D., Nestler, B., 2019. Understanding the influence of neighbours on the spheroidization of finite 3-dimensional rods in a lamellar arrangement: Insights from phase-field simulations. Lect. Notes Mech. Eng. 290–299.
Mittnacht, T., Kubendran Amos, P., Schneider, D., Nestler, B., 2021. Morphological stability of three-dimensional cementite rods in polycrystalline system: A phase-field analysis. J. Mater. Sci. Technol. 77, 252–268.
Moelans, N., Blanpain, B., Wollants, P., 2008. An introduction to phase-field modeling of microstructure evolution. CALPHAD 32 (2), 268–294.
Mullins, W., 1956. Two-dimensional motion of idealized grain boundaries. J. Appl. Phys. 27 (8), 900–904.
Murray, J.L., 1982. The Al-Mg (aluminum- magnesium) system. J. Phase Equilib. 3 (1), 60.
Nakajima, K., Apel, M., Steinbach, I., 2006. The role of carbon diffusion in ferrite on the kinetics of cooperative growth of pearlite: A multi-phase field study. Acta Mater. 54 (14), 3665–3672.
Nestler, B., Garcke, H., Stinner, B., 2005. Multicomponent alloy solidification: phase-field modeling and simulations. Phys. Rev. E 71 (4), 041609.
Nguyen, T.-T., Rethore, J., Yvonnet, J., Baietto, M.-C., 2017. Multi-phase-field modeling of anisotropic crack propagation for polycrystalline materials. Comput. Mech. 60 (2), 289–314.
Nichols, F., 1966. Coalescence of two spheres by surface diffusion. J. Appl. Phys. 37 (7), 2805–2808.
Nichols, F., Mullins, W., 1965. Morphological changes of a surface of revolution due to capillarity-induced surface diffusion. J. Appl. Phys. 36 (6), 1826–1835.
Nomura, Y., Minamoto, S., Nomoto, S., 2010. Simulations of solidification in Sn–3Ag–0.5 Cu alloys by the multi-phase-field method. ISIJ Int. 50 (12), 1920–1924.

Panteli, A., Robson, J., Brough, I., Prangnell, P., 2012. The effect of high strain rate deformation on intermetallic reaction during ultrasonic welding aluminium to magnesium. Mater. Sci. Eng. A 556, 31–42.
Park, M., Arróyave, R., 2009. Multiphase field simulations of intermetallic compound growth during lead-free soldering. J. Electron. Mater. 38 (12), 2525.
Park, M.S., Arroyave, R., 2010. Formation and growth of intermetallic compound Cu6Sn5 at early stages in lead-free soldering. J. Electron. Mater. 39 (12), 2574–2582.
Park, M., Arróyave, R., 2012. Concurrent nucleation, formation and growth of two intermetallic compounds (Cu6Sn5 and Cu3Sn) during the early stages of lead-free soldering. Acta Mater. 60 (3), 923–934.
Plaine, A., Gonzalez, A., Suhuddin, U., Dos Santos, J., Alcântara, N., 2015. The optimization of friction spot welding process parameters in AA6181-T4 and Ti6Al4V dissimilar joints. Mater. Des. 83, 36–41.
Plapp, M., 2011. Unified derivation of phase-field models for alloy solidification from a grand-potential functional. Phys. Rev. E 84 (3), 031601.
Qin, R., Bhadeshia, H., 2010. Phase field method. Mater. Sci. Technol. 26 (7), 803–811.
Raza, S.H., Klusemann, B., 2020. Multiphase-field modeling of temperature-driven intermetallic compound evolution in an Al-Mg system for application to solid-state joining processes. Modelling Simulation Mater. Sci. Eng..
Rosendo, T., Parra, B., Tier, M., Da Silva, A., Dos Santos, J., Strohaecker, T., Alcântara, N., 2011. Mechanical and microstructural investigation of friction spot welded AA6181-T4 aluminium alloy. Mater. Des. 32 (3), 1094–1100.
Saunders, N., 1990. A review and thermodynamic assessment of the Al-Mg and Mg-Li systems. CALPHAD 14 (1), 61–70.
Schaffnit, P., Apel, M., Steinbach, I., 2007. Simulation of ideal grain growth using the multi-phase-field model. In: Materials Science Forum, Vol. 558. Trans Tech Publ, pp. 1177–1181.
Schilling, C., dos Santos, J., 2004. Method and device for joining at least two adjoining work pieces by friction welding. US Patent 6, 722, 556.
Schneider, D., Schoof, E., Huang, Y., Selzer, M., Nestler, B., 2016. Phase-field modeling of crack propagation in multiphase systems. Comput. Methods Appl. Mech. Engrg. 312, 186–195.
Schneider, D., Schoof, E., Tschukin, O., Reiter, A., Herrmann, C., Schwab, F., Selzer, M., Nestler, B., 2018. Small strain multiphase-field model accounting for configurational forces and mechanical jump conditions. Comput. Mech. 61 (3), 277–295.
Schneider, D., Schwab, F., Schoof, E., Reiter, A., Herrmann, C., Selzer, M., Böhlke, T., Nestler, B., 2017. On the stress calculation within phase-field approaches: a model for finite deformations. Comput. Mech. 60 (2), 203–217.
Schneider, D., Tschukin, O., Choudhury, A., Selzer, M., Böhlke, T., Nestler, B., 2015. Phase-field elasticity model based on mechanical jump conditions. Comput. Mech. 55 (5), 887–901.
Schoof, E., Amos, P.K., Schneider, D., Nestler, B., 2020. Influence of stress-free transformation strain on the autocatalytic growth of bainite: a multiphase-field analysis. Materialia 9, 100620.
Silhavy, M., 2013. The Mechanics and Thermodynamics of Continuous Media. Springer Science & Business Media.
Smerd, R., 2005. Constitutive Behavior of Aluminum Alloy Sheet at High Strain Rates (Master's thesis). University of Waterloo.
Smith, G.W., White, J.L., Buechler, M., 1985. Mesophase/isotropic phase interfacial energy: Determination from coalescence kinetics of mesophase pitch. Carbon 23 (1), 117–121.
Steinbach, I., 2009. Phase-field models in materials science. Modelling Simulation Mater. Sci. Eng. 17 (7), 073001.
Steinbach, I., Apel, M., 2006. Multi phase field model for solid state transformation with elastic strain. Physica D 217 (2), 153–160.
Steinbach, I., Pezzolla, F., 1999. A generalized field method for multiphase transformations using interface fields. Physica D 134 (4), 385–393.
Steinbach, I., Pezzolla, F., Nestler, B., Seeßelberg, M., Prieler, R., Schmitz, G.J., Rezende, J.L., 1996. A phase field concept for multiphase systems. Physica D 94 (3), 135–147.
Steinmetz, P., Hötzer, J., Kellner, M., Dennstedt, A., Nestler, B., 2016. Large-scale phase-field simulations of ternary eutectic microstructure evolution. Comput. Mater. Sci. 117, 205–214.
Suhuddin, U., Fischer, V., Dos Santos, J., 2013. The thermal cycle during the dissimilar friction spot welding of aluminum and magnesium alloy. Scr. Mater. 68 (1), 87–90.
Suhuddin, U., Fischer, V., Kroeff, F., Dos Santos, J., 2014. Microstructure and mechanical properties of friction spot welds of dissimilar AA5754 Al and AZ31 Mg alloys. Mater. Sci. Eng. A 590, 384–389.
Tozaki, Y., Uematsu, Y., Tokaji, K., 2007. Effect of processing parameters on static strength of dissimilar friction stir spot welds between different aluminium alloys. Fatigue Fract. Eng. Mater. Struct. 30 (2), 143–148.
Yamamoto, N., Liao, J., Watanabe, S., Nakata, K., 2009. Effect of intermetallic compound layer on tensile strength of dissimilar friction-stir weld of a high strength Mg alloy and al alloy. Mater. Trans. 50 (12), 2833–2838.
Yan, J., Xu, Z., Li, Z., Li, L., Yang, S., 2005. Microstructure characteristics and performance of dissimilar welds between magnesium alloy and aluminum formed by friction stirring. Scr. Mater. 53 (5), 585–589.
Yang, X., Fu, T., Li, W., 2014. Friction stir spot welding: a review on joint macro-and microstructure, property, and process modelling. Adv. Mater. Sci. Eng. 2014.
Yang, C., Wu, C., Zhao, J., 2021. Numerical prediction of intermetallic compounds thickness in friction stir welding of dissimilar aluminum/magnesium alloys. Acta Metall. Sin. (Engl. Lett.) 1–11.
Zhong, Y., Yang, M., Liu, Z.-K., 2005. Contribution of first-principles energetics to Al–Mg thermodynamic modeling. CALPHAD 29 (4), 303–311.
Zuo, Y., Chang, Y., 1993. Thermodynamic calculation of the Al-Mg phase diagram. CALPHAD 17 (2), 161–174.